Dual actions of osteoclastic-inhibition and osteogenic-stimulation through strontium-releasing bioactive nanoscale cement imply biomaterial-enabled osteoporosis therapy

Na-Hyun Lee[1,2], Min Sil Kang[1,2], Tae-Hyun Kim[1,2], Dong Suk Yoon[1,2], Nandin Mandakhbayar[1,2], Seung Bin Jo[1], Hye Sung Kim[1,5,6,7,8], Jonathan C. Knowles[2,3,4,7], Jung-Hwan Lee [1,2,5,6,7,8,9,*] and Hae-Won Kim [1,2,5,6,7,8,9,*]

[1]Institute of Tissue Regeneration Engineering (ITREN), Dankook University, Cheonan 31116, Republic of Korea

[2]Department of Nanobiomedical Science and BK21 NBM Global Research Center for Regenerative Medicine, Dankook University, Cheonan 31116, Republic of Korea

[3]Division of Biomaterials and Tissue Engineering, UCL Eastman Dental Institute, 256 Grays Inn Road, London WC1X 8LD, UK

[4]The Discoveries Centre for Regenerative and Precision Medicine, UCL Campus, London, UK

[5]Department of Biomaterials Science, School of Dentistry, Dankook University, Cheonan 31116, Republic of Korea

[6]Department of Regenerative Dental Medicine, School of Dentistry, Dankook University, Cheonan 31116, Republic of Korea

[7]Cell & Matter Institute, Dankook University, Cheonan 31116, Republic of Korea

[8]Mechanobiology Dental Medicine Research Center, Cheonan 31116, Republic of Korea

[9]UCL Eastman-Korea Dental Medicine Innovation Centre, Dankook University, Cheonan 31116, Republic of Korea

---

[*]**Correspondence to:**

J.-H. Lee (E-mail: ducious@gmail.com) & H.-W. Kim (kimhw@dku.edu)

Tel.: +82 41 550 3081, Fax.: +82 41 559 7839

Institute of Tissue Regeneration Engineering (ITREN), Dankook University, Republic of Korea

Graphical abstract

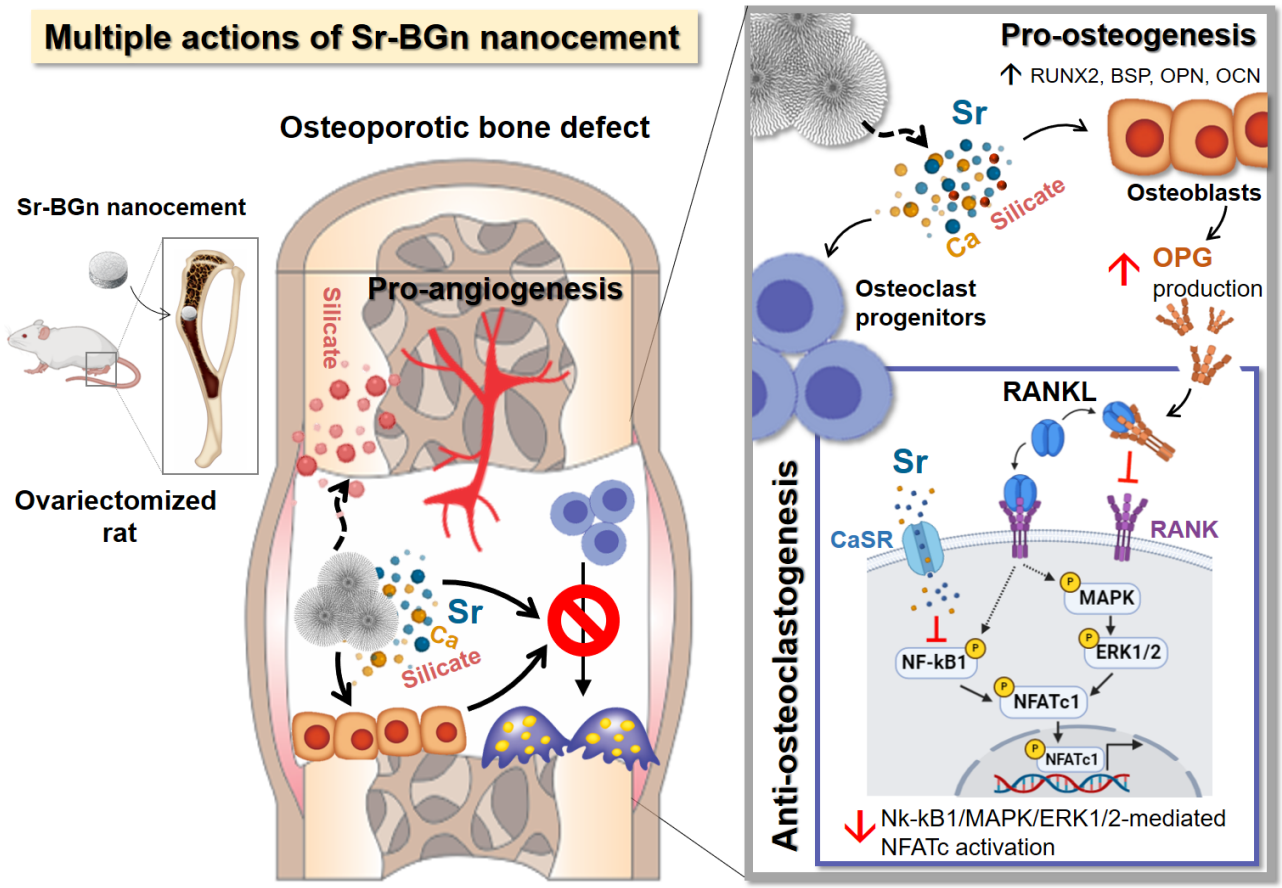

Abstract

Repair of defective hard-tissues in osteoporotic patients faces significantly challenges with limited therapeutic options. Although biomedical cements are considered promising materials for healthy bone repair, their uses for healing osteoporotic fracture are clinically limited. Herein, strontium-releasing-nanoscale cement was introduced to provide dual therapeutic-actions (pro-osteogenesis and anti-osteoclastogenesis), eventually for the regeneration of osteoporotic bone defect. The Sr-nanocement hardened from the Sr-doped nanoscale-glass particles was shown to release multiple ions including silicate, calcium and strontium at doses therapeutically relevant over time. When the Sr-nanocement was treated to pre-osteoblastic cells, the osteogenic mRNA level (*Runx2, Opn, Bsp, Ocn*), alkaline phosphatase activity, calcium deposition, and target luciferase reporter were stimulated with respect to the case with Sr-free-nanocement. When treated to pre-osteoclastic cells, the Sr-nanocement substantially reduced the osteoclastogenesis, such as osteoclastic mRNA level (*Casr, Nfatc1, c-fos, Acp, Ctsk, Mmp-9*), tartrate-resistant acid trap activity, and bone resorption capacity. In particular, the osteoclastic inhibition resulted in part from the interactive effect of osteoblasts which were activated by the Sr-nanocement, *i.e*., blockage of RANKL (receptor activator of nuclear factor-κB ligand) binding by enhanced osteoprotegerin and the deactivated *Nfatc1*. The Sr-nanocement, administered to an ovariectomized tibia defect (osteoporotic model) in rats, exhibited profound bone regenerative potential in cortical and surrounding trabecular area, including increased bone volume and density, enhanced production of osteopromotive proteins, and more populated osteoblasts, together with reduced signs of osteoclastic bone resorption. These results demonstrate that Sr-nanocement, with its dual effects of osteoclastic inhibition and osteogenic-stimulation, can be considered an effective nanotherapeutic implantable biomaterial platform for the treatment of osteoporotic bone defects.

Keywords: Strontium doped nanoglass particles; Osteoporosis treatment; Osteoclastic inhibition; Osteogenic stimulation; Osteoblast-osteoclast interaction

1. Introduction

Bone is continuously remodeled, which allows to maintain bone strength as well as calcium homeostasis [1, 2]. If the interplay between bone-forming osteoblasts and bone-resorbing osteoclasts is dysregulated, there is an increase or, mostly, decrease in bone mass, called osteoporosis which commonly occurs among postmenopausal woman or elderly man [3-5]. The reduced bone mineral density from osteoporotic patients causes premature fracture which is complicated by increased morbidity, mortality, and social costs [6, 7]. Fractures can occur at various locations of skeleton such as hip and tibia, and the bone forming activity related with accelerated osteoclast behaviors can delay the regeneration of defective bone [8, 9].

Osteoporosis patients are generally treated preventively with bisphosphonates to reduce fracture risk, which are well-known anti-resorptive drugs to inhibit osteoclast functionality [10-18]. However, long-term administration of bisphosphonate drugs to osteoporotic fractures has been questioned on the fracture healing [19]. As alternatives, anabolic drugs such as parathyroid hormone and their derivatives (teriparatide) have also been used to stimulate cellular bone-forming behaviors and have displayed accelerated fracture healing, but the efficacy was suboptimal with high cost in clinical settings [20]. On the other hand, strontium (Sr) ranelate, a Sr(II) salt of ranelic acid, has been introduced to prevent osteoporosis and regenerate osteoporotic bone defect as a 'dual action bone agent', *i.e.,* increasing new bone formation by osteoblasts and, simultaneously, diminishing bone resorption by osteoclasts through Sr ions released [8, 16, 21-29]. Even though the therapeutic roles of Sr ranelate were proven in various osteoporotic patients in terms of strengthening intrinsic bone quality and healing, its use has been discontinued since 2016-2017 due to accumulated side effects such as venous thromboembolism and life-threatening allergic reactions by oral systemic administration [30, 31]. To tackle this issue raised on Sr ranelate associated with systemic delivery, Sr-ranelate- or Sr-loaded biomaterials (in scaffold, micro-particle, or cement forms) have been proposed to release Sr ions sustainably that might help regenerating osteoporotic bone while relieving overdose burdens [32-44].

Recently, nanoscale osteogenic cement, called nanocement, was newly produced from nanoglass particles for bone regeneration due to its unique nanoscale morphology and physico-chemical and biological properties such as hardening ability, high surface area, protein loading capacity, *in vitro* bioactivity, and *in vivo* osteoinductive properties [45, 46]. Of note, the nanoscale cement can incorporate therapeutic ions (*e.g.*, cobalt, copper, zinc, silver), which further released to exert anti-bacterial, angiogenic or wound healing effects [37, 46-51]. In light of this, we consider Sr ions can also be incorporated into the nanoscale cement which is ultimately effective in the treatment of osteoporosis while preserving the bioactive nanocement properties, such as self-hardening, defect filling, and the cell/tissue compatibility and activity [17, 52, 53].

In particular, the prepared Sr-doped nanoscale cement was considered to exert 'dual therapeutic actions' of Sr ions, *i.e.*, promoting osteoblasts while deactivating osteoclasts [22, 47]. To test this, we first examined the osteogenic stimulation of the Sr-nanocement in terms of the expression of osteogenic genes and proteins, and

cellular mineralization. Next, we analyzed the osteoclastogenic inhibition by the expression of osteoclastic genes, actin ring formation of multinucleated cells, and osteoclastic enzymatic activity. Further, we investigated the interplay of osteoblasts/osteoclasts mediated by Sr-nanocement by means of osteoprotegerin (OPG)/receptor activator of nuclear factor (NF)-ϰB ligand (RANKL) interactions and the related intracellular signaling pathways. Lastly, we addressed if the Sr-nanocement administered to an osteoporotic bone defect model in rats would be effective in enhancing the bone repair process. This study is considered to provide a potential nanoscale self-hardening implantable biomaterial platform that exhibits dual therapeutic actions in treating osteoporotic bone healing.

2. Results and Discussion

2.1. Hardening process and characteristics of Sr-nanocement

The nanoscale glass powders containing Sr (termed 'Sr-BGn') or not (termed 'BGn') were first synthesized by a sol-gel method for the preparation of nanocements [45]. The morphology of the nanopowders, as observed by FE-SEM and TEM, revealed a mesoporous structure with an average size of 247.2 (±29.5) nm (**Fig. 1A-i,ii**). The FT-IR and XRD analyses of the nanopowders confirmed chemical bands and phase typical of silicate-based glass (**Fig. S1A,D**). The TEM-EDS analysis **(Fig. S1C)** confirmed the Si:Ca:Sr ratio of 85.2:10.1:4.7, a value similar to the stoichiometry of 85Si-10Ca-5Sr glass. The BET analysis displayed highly mesoporous characteristics; surface area (693 m^2/g), average pore size (6.64 nm) and total pore volume (0.61 cm^3/g) (**Fig. 1A-iii**), and the surface ξ-potential was measured to be slightly negative (-15.6 mV). The morphological and chemical characteristics of the Sr-doped nanopowders were thus found to be similar to those of Sr-free nanopowders (BGn) (as shown in **Fig. S1**).

Next, the prepared Sr-BGn were mixed with a liquid phase which was allowed to set for preparing nanocement (termed 'Sr-BGnC') (setting procedure depicted in **Fig. 1B-i**). As a liquid phase, distilled water (DW) or 2.5wt% NaH_2PO_4 was used to find proper nanopowder-to-liquid ratio (P/L ratio) and setting time (t_{set}). Setting was possible with P/L ratio in the range of 0.3~0.5, with which the t_{set} was recorded to be 40-240 min (**Fig. 1B-ii**). The t_{set} became shortened when NaH_2PO_4 (*vs*. DW) was used and P/L ratio increased. The setting condition for further experiments was chosen at P/L ratio of 0.4 using NaH_2PO_4 with which the setting time was ~60 min. The FE-SEM microstructure of the hardened nanocement sample showed the initial morphology of nanoparticles (**Fig. 1B-iii**). A closer examination by TEM revealed the formation of nanoscale aggregates (arrows) on the surface of initial nanoparticles (**Fig. 1B-iv**), a phenomenon similar to the case in Sr-free nanocement (**Fig. S2**). As illustrated in **Fig. 1B-v**, the setting mechanism of the Sr-nanocement can be explained as the dissolution-reprecipitation process [45]. In detail, the ions (Ca, Sr, silicate) leach out from the nanoparticles in an aqueous medium (NaH_2PO_4 or DW), and the released ions, together with the ions in the

medium (*e.g.*, phosphate), precipitate on the surface of nanoparticles. The precipitates (nanoscale aggregates noted in Fig. 1B-iv) are composed of Ca-Sr-Si-(P) oxide and in an amorphous phase (as revealed in the XRD data in **Fig. S3**) which enable the nanoparticles to make networks and harden.

The nanocements were shown to be highly reactive in contact with an ionic fluid, particularly with a simulated body fluid (SBF). When immersed in SBF, apatite-like nanocrystallites were quickly and profoundly formed (shown in **Fig. 1C-i**); this acellular mineralization (apatite formation) generally implies a high bioactivity of materials developed for bone. Of note, the mineralized nanocement showed highly mesoporous characteristics based on the BET analysis; the surface area increased with increasing SBF immersion time while preserving the mesopores size (**Fig. 1C-ii**, and **Fig. S4A**). The apatite formation increased with immersion time (**Fig. S4B,C**). For the ion releasing test of nanocements, Tris-buffer was used due to its neutral pH and high buffering capacity without any intervention of ion components [54-56]. The Sr-nanocement could release multiple ions over 14 days including silicate, Ca, and Sr, as measured by ICP-AES (**Fig. 1C-iii**). Specifically, the three different ions were released slowly from the Sr-BGnC over 14 days; the silicate and Ca release was similar to that observed in BGnC while the Sr release was a unique phenomenon in Sr-BGnC. Collectively, the Sr-nanocement hardened from Sr-doped nanoglass powders showed highly mesoporous structure, acellular mineralization capacity, and the release of multiple ions including silicate, Ca, and particularly Sr that were considered to exert therapeutic effects on osteoblastic and osteoclastic cells.

To examine the effects of nanocements on the *in vitro* cell behaviors, ionic-extracted media were used to investigate ionic effects of nanocements (BGnC, Sr-BGnC) irrespective of surface properties (*e.g.,* topography, chemistry). For this, the nanocement samples were extracted in a culture medium for 24 h while shaking gently. The resultant ionic-extract concentrations were recorded: 22.73 (Sr-BGnC) and 21.50 ppm (BGnC) for silicate, 74.66 (Sr-BGnC) and 86.24 ppm (BGnC) for Ca, and 12.18 ppm (Sr-BGnC) for Sr (as summarized in **Table S1**). Also, free Sr ions were prepared from $SrCl_2$ for the comparison study with the extracts from Sr-BGnC. The nanocement extracts were then serially diluted (down to 1/128) for the cell cultures; the ionic doses used for the cultures were considered to show some therapeutic effects such as osteogenesis, angiogenesis, and/or anti-osteoclastogenesis [47, 57-59]. First, the extracts were treated to various kinds of cells including osteoblastic cells (MC3T3-E1) and osteoclastic cells (RANKL-induced RAW264.7) for up to 2 days to confirm the effects on cellular viability. All the extracts were found to exert little toxicity to the series of cells tested (**Fig. S5**). Thus, the original extract was used for further *in vitro* culture studies.

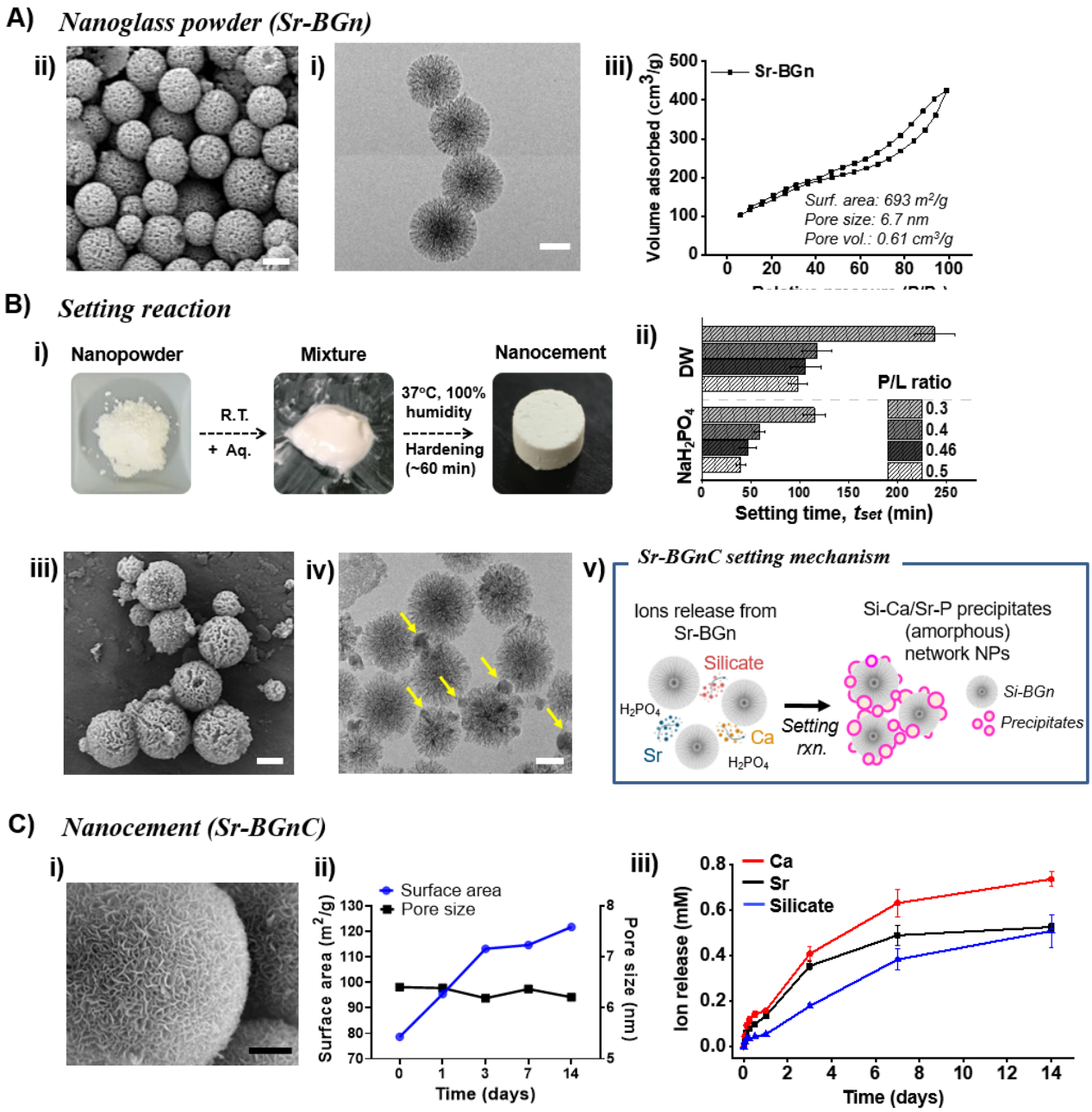

Figure 1. Characteristics of the strontium-doped nanocement. (A) Characteristics of nanoglass powder, Sr-BGn; (i,ii) nanostructure observed by FE-SEM and TEM (scale bar = 100 nm) and (iii) BET nitrogen adsorption/desorption curves displaying highly mesoporous characteristics (surface area, pore size, and pore volume are included in inset). (B) Setting of Sr-BGn; (i) hardening procedure, (ii) setting time (t_{set}) recorded with different P/L ratio and liquid type, (iii) FE-SEM and (iv) TEM image, revealing nano-precipitates on the surface of the Sr-BGn (arrows), and (v) schematic illustration of the setting mechanism of Sr-BGnC. (C) Properties of Sr-nanocement, Sr-BGnC; (i) TEM image of Sr-BGnC after immersion in SBF for 14 days (scale bar = 500 nm), showing apatite-like nanocrystallites formation, (ii) BET analysis indicating highly mesoporous characteristics of the mineralized nanocement, and (iii) release profiles of ions from Sr-BGnC measured by ICP-AES for up to 14 days (in Tris-HCl buffer at pH 7.4).

2.2. Sr-nanocement stimulates osteogenesis

After the cell viability with the nanocements was confirmed, the effects on osteogenic responses were examined with MC3T3-E1 cells. The nanocement extracts were treated to the cells under conditions supplemented with osteoblast differentiation factors (OBDF). Growth medium (GM) was also used as a negative control. First, the osteogenic transcriptional activity of *Runx2* and *Ocn* was investigated using *Runx2*-responsive (6XOSE-luciferase) and *Ocn* promoter-responsive (OG2-luciferase) artificial luciferase reporter plasmids [60-62] (**Fig. 2A**). Both luciferase activities were enhanced in Sr-BGnC than in BGnC and Sr ion control. Next, the expression of osteoblast-related genes (*Runx2, Bsp, Opn, and Ocn*) at days 3, 7 and 14 was shown to increase in nanocement groups (both BGnC and Sr-BGnC) with respect to nanocement-free group (OBDF), and the stimulating effect was more significant in the cells treated with Sr-BGnC, implying a possible osteogenic synergism between Sr and silicate (or Ca) ions (**Fig. 2B**). Interestingly, Sr-BGnC showed highly up-regulated gene expressions, with more than 6 times of the Sr ion counterpart made from $SrCl_2$; in fact, the $SrCl_2$ was previously shown to be osteogenic and anti-osteoclastogenic elsewhere [11, 63-65]. Lastly, the ALP (violet color) and ARS staining (red color), assessed at days 7, 14, 21, and 28, demonstrated more enhanced ALP activity and cellular mineralization in Sr-BGnC than in BGnC and Sr ion counterpart, indicating the possible osteogenic stimulation of ions released from Sr-BGnC at intermediate and terminal differentiation stage (**Fig. 2C,D**). Furthermore, the rat bone marrow derived mesenchymal stem cells (rMSCs) tested with the nanocements were shown to be stimulated (ALP and ARS stains) in a similar manner to the MC3T3-E1 cells (supplementary data, **Fig. S6**), supporting the osteogenic differentiation potential of Sr-BGnC. Taken together, Sr-BGnC induced higher osteogenesis than BGnC, possibly due to the osteogenic stimulating effects of multiple ions (both Sr and silicate/Ca) released from the Sr-BGnC [36, 63-68].

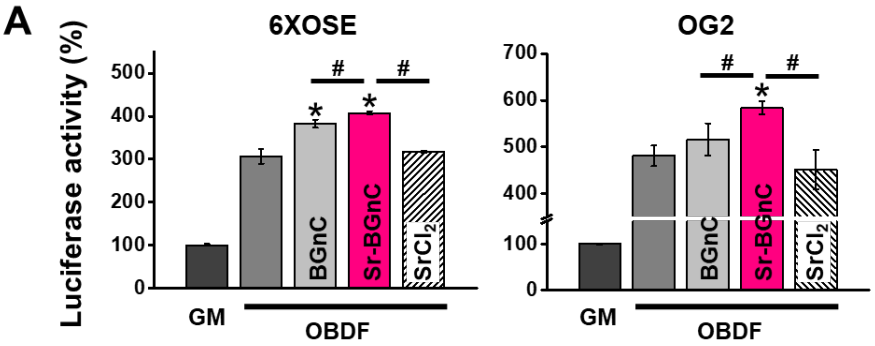

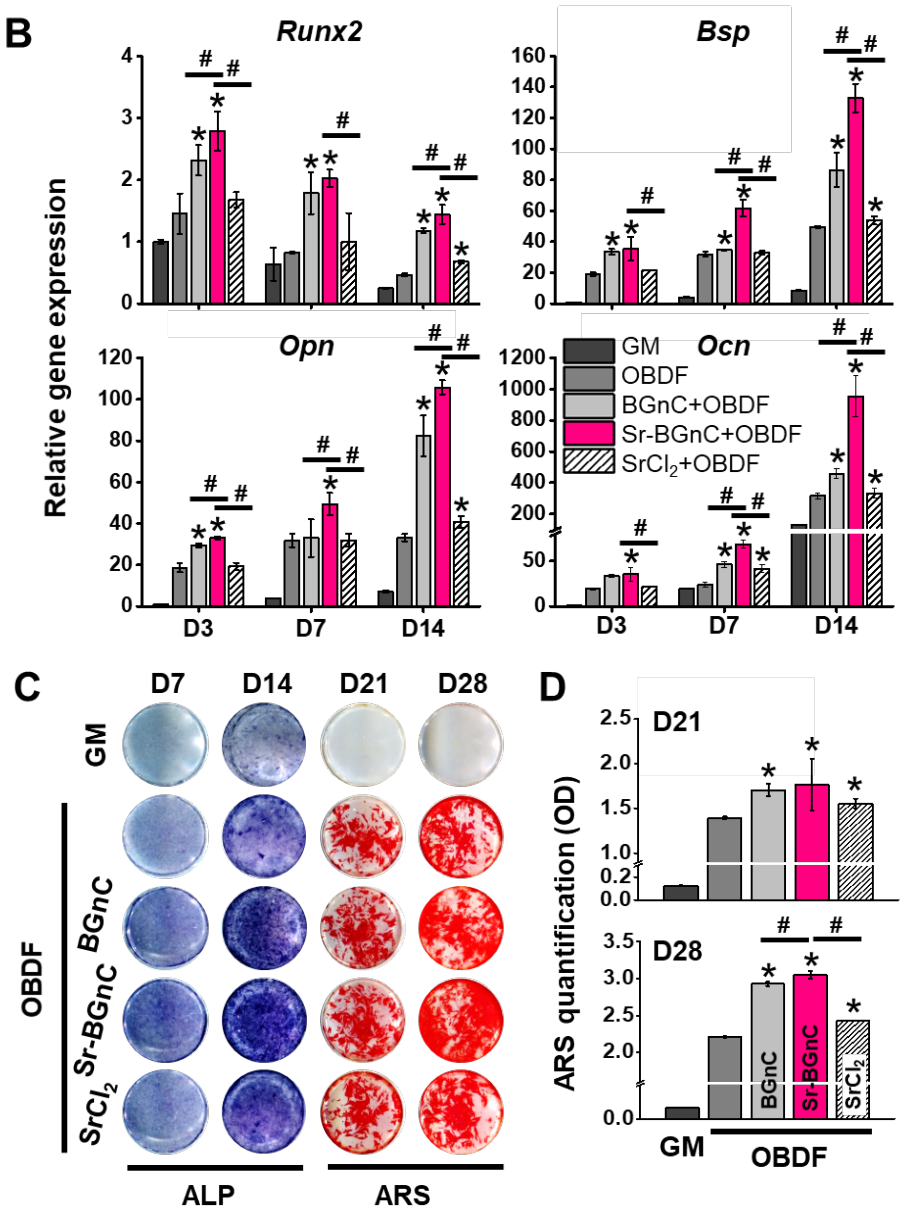

Figure 2. Osteogenesis capacity of Sr-BGnC in pre-osteoblastic MC3T3-E1 cells. Cells were cultured in growth medium (GM), GM supplemented with osteoblast differentiation factors (OBDF), or GM with OBDF containing extracts of BGnC, Sr-BGnC or $SrCl_2$. (A) Osteogenic transcriptional activity of *Runx2* and *Ocn* examined by luciferase reporter assay. Cells were transfected with luciferase reporter plasmids encoding either *Runx2*-responsive 6XOSE or *Ocn* promotor-responsive OG2. In addition, cells were co-transfected with Renilla, a luciferase control reporter vector, for normalization. (B) Expression levels of osteogenesis-related genes including *Runx2, Bsp, Opn and Ocn* in MC3T3-E1 cells cultured for 3, 7, or 14 days. (C) ALP staining (violet) at days 7 and 14 and ARS staining (red) at days 21 and 28, and (D) the quantification of the calcium deposits at days 21 and 28. * indicates $p<0.05$ *versus* OBDF group and # indicates $p<0.05$ between groups (n = 3).

2.3. Sr-nanocement inhibits osteoclastogenesis

For the osteoclastic differentiation study, RAW264.7 cells were cultured under conditions supplemented with

osteoclast differentiation factors (OCDF) that involves RANKL (and also M-CSF and TGF-β). After 3 days of culture with or without nanocement extracts, the expression of osteoclast-related genes, including calcium sensing receptor (*Casr*), osteoclast transcription factors (*Nfatc1, c-fos*), and bone-resorption enzymes (*Acp5, Ctsk,* and *Mmp9*) [11, 47, 64, 69, 70], was then analyzed (**Fig. 3A**). The Sr-BGnC suppressed the expression of all osteoclast-related genes tested more significantly than the BGnC and Sr ion control.

Next, the formation of actin ring, a typical actin structure essential for bone resorption by active osteoclasts, was visualized by confocal microscopy. Actin ring formation was less noticeable in Sr-BGnC than in the other groups (**Fig. 3B**). The osteoclastic enzymatic activity, as analyzed by TRAP staining, was substantially reduced in Sr-BGnC, with significantly decreased area of TRAP (+) multinucleated osteoclasts (**Fig. 3C**). Also, the bone resorption test, assessed on a mineral coating plate, revealed significantly reduced total resorption area (pit area) in Sr-BGnC (**Fig. 3D**).

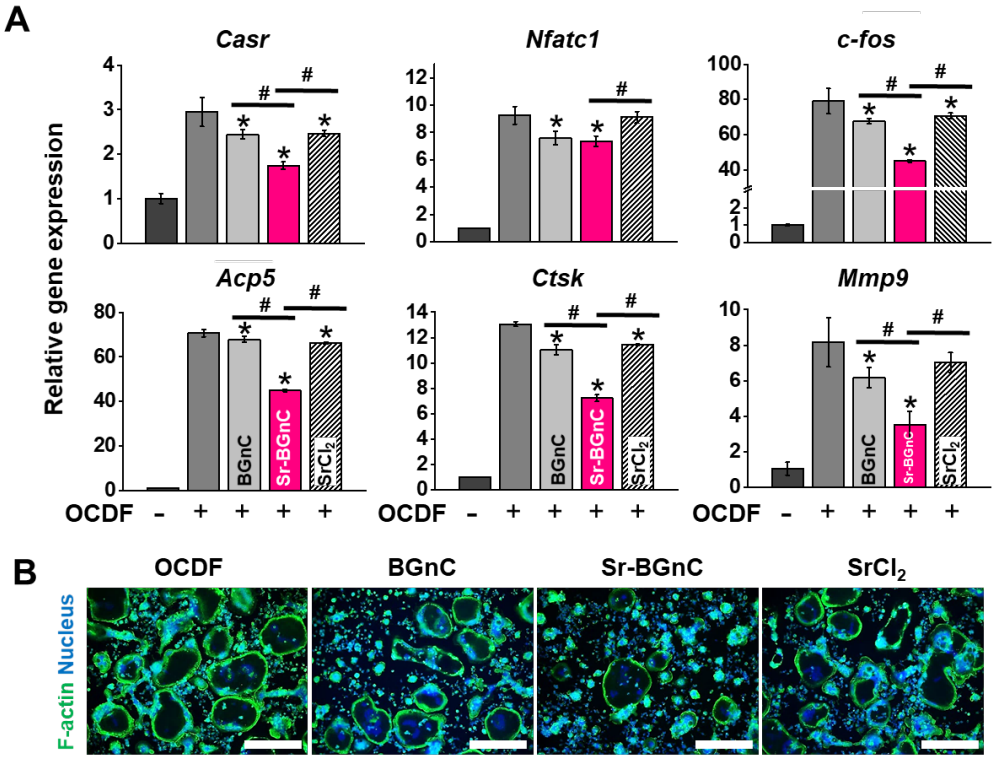

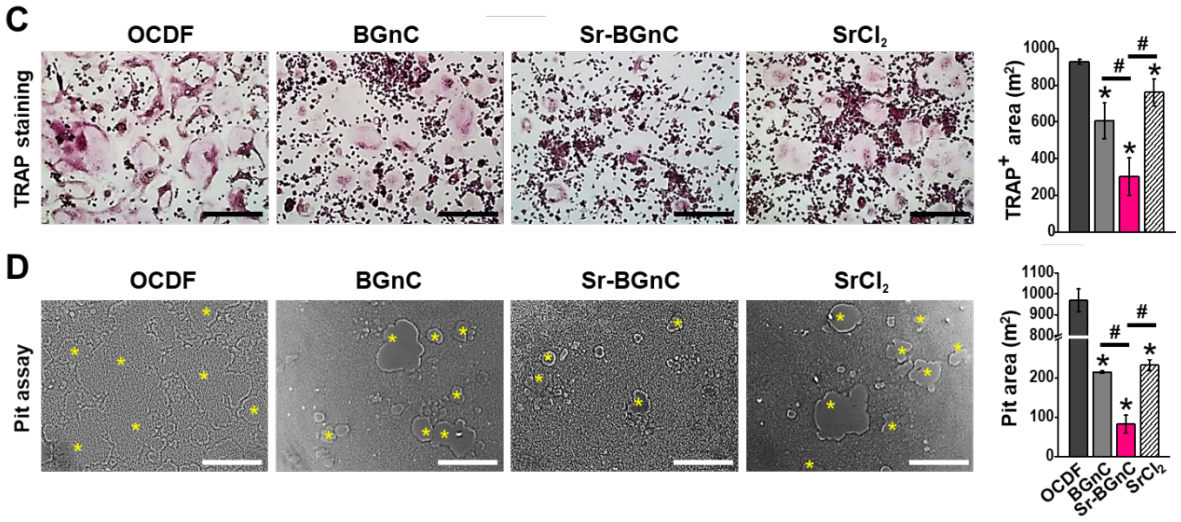

Figure 3. Anti-osteoclastic differentiation effect of Sr-BGnC in pre-osteoclastic RAW264.7 cells. Cells were cultured for 6 days in the presence of osteoclast differentiation factors (OCDF) containing RANKL, M-CSF and TGF-β. (A) Expression levels of osteoclast-related genes including *Casr, Nfatc1, c-fos, Acp5, Ctsk,* and *Mmp9* at day 3. (B) Formation of actin rings stained by Phalloidin at day 6 (scale bar = 175 μm). (C) Osteoclastic enzymatic activity evaluated by TRAP staining (pinkish) and pit (asterisk) formation assay associated with bone resorption capacity at day 6 (scale bar = 175 μm). (D) TRAP positive area and pit area measured by Image J based on the optical images. * indicates $p<0.05$ *versus* OCDF group and # indicates $p<0.05$ between groups (n = 3).

2.4. Sr-nanocement inhibits osteoclastogenesis through regulation of osteoblasts signaling

The inhibitory effect of Sr-BGnC on osteoclastogenesis was further interpreted by the interactions with osteoblasts. For this, the MC3T3-E1 cells were cultured with nanocement extract in OBDF or GM for 6 days and then the conditioned medium was transferred every other day to the RAW264.7 cultures (in OCDF) which lasted for up to 6 days (thus 8, 10, and 12 days from the start of osteogenic differentiation), as illustrated in **Fig. 4A**. First, the *Nfatc1* osteoclastic transcriptional activity was examined by *Nfatc1*-luciferase reporter assay (**Fig. 4B**). Results showed that the activity was significantly down-regulated in the groups treated with the osteoblastic medium co-cultured with nanocements, particularly with Sr-BGnC. The treatment with Sr ion counterpart was also effective albeit less than the nanocement groups. Next, the expression of osteoclast-related genes was analyzed by qPCR (**Fig. 4C**). The expression of *Casr, Nfatc1, c-fos, Acp5, Ctsk*, and *Mmp9* was significantly down-regulated by the treatment of conditioned medium with nanocements or Sr ion counterpart. The analysis of TRAP activity also showed similar effects by the nanocements (**Fig. 4D**). The TRAP (+) cells stained to be multinucleated osteoclasts (**Fig. 4E**) and the substrate pit formation associated with bone resorption capacity (**Fig. 4F**) were significantly reduced by the treatment of conditioned medium with nanocements or Sr ion counterpart in the order of the effect: Sr-BGnC >> BGnC > Sr ion.

Taken together, the inhibitory effects on osteoclastic differentiation and functional activity through the osteoblasts-conditioned medium imply that there exists possible molecular signaling of osteoblasts linked to

the process of osteoclastogenesis [71]. Of note, the conditioned medium of osteoblasts treated with nanocements successfully hindered the osteoclasts formation and their mineral resorption activity, demonstrating the potential anti-osteoclastic role played indirectly by the nanocements through activation of osteoblasts. It is further worth noting that firstly, the osteoclastic inhibition by the conditioned medium with nanocements was more effective than by the direct treatment of nanocements, and secondly, the effects of BGnC (Sr-free) was more pronounced in the osteoblasts-conditioned medium experiments. Collectively, the Sr-BGnC were proven to be highly effective in inhibiting osteoclastogenesis indirectly through the regulation of osteoblasts as well as directly to osteoclasts, presumably resulting from the multiple ions released, and the findings suggest that the roles of Sr-BGnC played in osteoblastic activation and osteoclastic suppression should be interpreted in the context of osteoblasts-osteoclasts interactions.

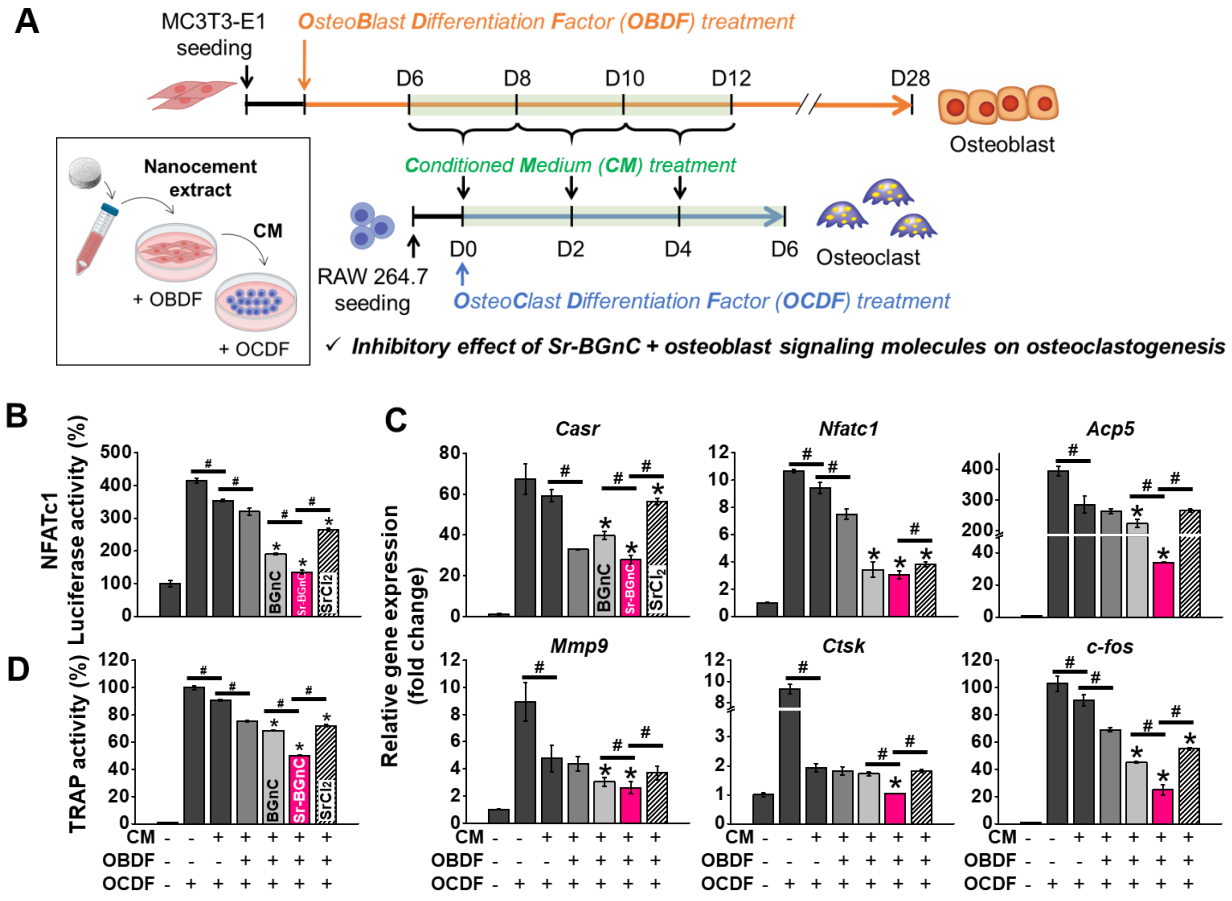

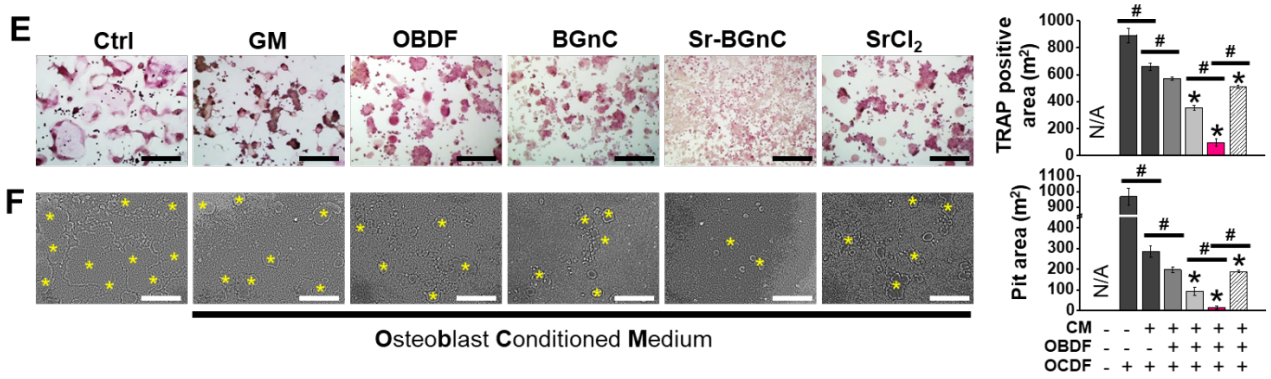

Figure 4. Inhibitory effect of Sr-BGnC in combination with osteoblastic signaling molecules on osteoclastogenesis of RAW264.7. Culture supernatant of MC3T3-E1 cells undergoing the osteoblast differentiation was collected as a conditioned medium. RAW264.7 cells were differentiated in the presence of osteoclast differentiation factors for 6 days. The conditioned medium was treated to the RAW264.7 cells during the 6 days of the differentiation. (A) Schematic timeline of the conditioned medium treatment. (B-F) Evaluations of the osteoclast differentiation by examining osteoclastic transcriptional activity in RAW264.7 cells transfected with *Nfatc1*-luciferase plasmids at day 3 (B), the expression levels of osteoclast-related genes at day 3 (C), TRAP activity (D), TRAP staining (E) and pit formation assay (F) at day 6 with quantitative analysis results. * indicates $p<0.05$ *versus* CM condition and # indicates $p<0.05$ between groups (n = 3). CM; conditioned medium, OBDF; osteoblast differentiation factor, and OCDF; osteoclast differentiation factor.

At this point, the candidate molecules engaged in the interplay between osteoblasts and osteoclasts were then analyzed. It is known that osteoprotegerin (OPG) and soluble RANKL are two key molecules involved in the osteoclasts-osteoblasts communication; while soluble RANKL can activate osteoclasts formation, OPG can bind to RANKL receptor (RANK) and inhibit osteoclasts differentiation as a competitive inhibitor [72-75]. The osteoclasts-osteoblasts communication through molecular interactions with OPG and RANKL is schematically shown in **Fig. 5A**. Of the two molecules, here we focused on OPG as the RANKL was already supplemented at high concentrations in osteoclastic differentiaion conditions. As illustrated in **Fig. 5B-i**, the OPG produced by oseoblasts can be either degraded or consumed by osteoclasts during the step-wise cultures. Considering this, the OPG amount during the cultures under different treatment conditions was measured. First, the OPG amount present in various conditioned media was compared (**Fig. 5B-ii**). Compared to the growth condition (GM), the osteoblast differentiation condition (OBDF) greatly increased the OPG secretion. When cultured additionally with nanocements or $SrCl_2$, the OPG production became significantly increased in the order: Sr-BGnC > $SrCl_2$ > BGnC, indicating the ions from nanocements or $SrCl_2$ might have a stimulatory effect on OPG production by osteoblasts. Approximately 5-7 ng of OPG was more produced in those groups *versus* OBDF group at day 12. The osteoblasts-conditioned medium was then used for the osteoclasts cultures and the OPG remained in the medium was further analyzed to identify how much OPG was involved in the inhibition of osteoclastic differentiation during culture for up to 6 days (**Fig. 5B-iii**). Results showed that the OPG remained the highest in the Sr-BGnC-mediated conditioned medium group by differences of ~5-8 ng from the other groups at day 6, which however, somewhat deviated from our expectation. We thus further

calculated the OPG% (consumed or degraded) based on the produced and remained OPG contents (**Fig. 5B-iv**). The results showed that the difference among groups was more apparent with time, and the OPG% became lowered in the groups treated with conditioned medium in the order: OCDF control >> $SrCl_2$ > BGnC >> Sr-BGnC. A recent report demonstrated that the OPG progressively degraded particularly in the matured osteoclasts due to the significantly increased enzymatic activity, attenuating the inhibitory role of OPG in osteoclasts signaling [72] ; therefore, the OPG content particularly at later time point is considered to mirror this degradation issue.

Given that the OPG% would be either consumed or degraded, data thus need a careful interpretation; the consumed OPG is involved in the osteoclastic inhibition by blocking RANKL recognition by osteoclasts (mainly in the groups with predominant anti-osteoclastic actions like Sr-BGnC) whereas the degraded OPG is due to increased enzymatic action of the activated osteoclastogenesis (mainly in the groups with predominant osteoclastic actions like OCDF); recalling from illustration in **Fig. 5B-i**. Therefore, it is considered that the significantly lowered OPG% in Sr-BGnC might be due mainly to the consumed OPG whereas the decreased OPG% (*vs*. GM control) might result from the degradation by activated osteoclasts.

As witnessed, the roles of Sr-BGnC played in the inhibition of osteoclasts are bilateral; directly on osteoclasts and indirectly though osteoblasts signaling, and the events are dynamic along the osteoclastogenesis progress. Next, the intracellular signaling pathways underlying the osteoclastogenesis inhibitory events were identified, by western blot analysis of possible key signaling molecules including NFATc1, NF-kB, MAPK, ERK1/2, and their phosphorylated forms. The NF-kB/MAPK/ERK1/2-mediated NFATc1 activation is a well-known osteoclast differentiation signaling pathway [76-78]. All the intracellular signaling molecules considered were shown to be responsive similarly, *i.e*., significantly down-regulated by the osteoblasts-conditioned medium, and particularly in the group pretreated with Sr-BGnC (**Fig. 5C**), suggesting that Sr-BGnC inhibited osteoclast differentiation through the deactivation of NF-kB/MAPK/ERK1/2-mediated NFATc1 transcriptional process.

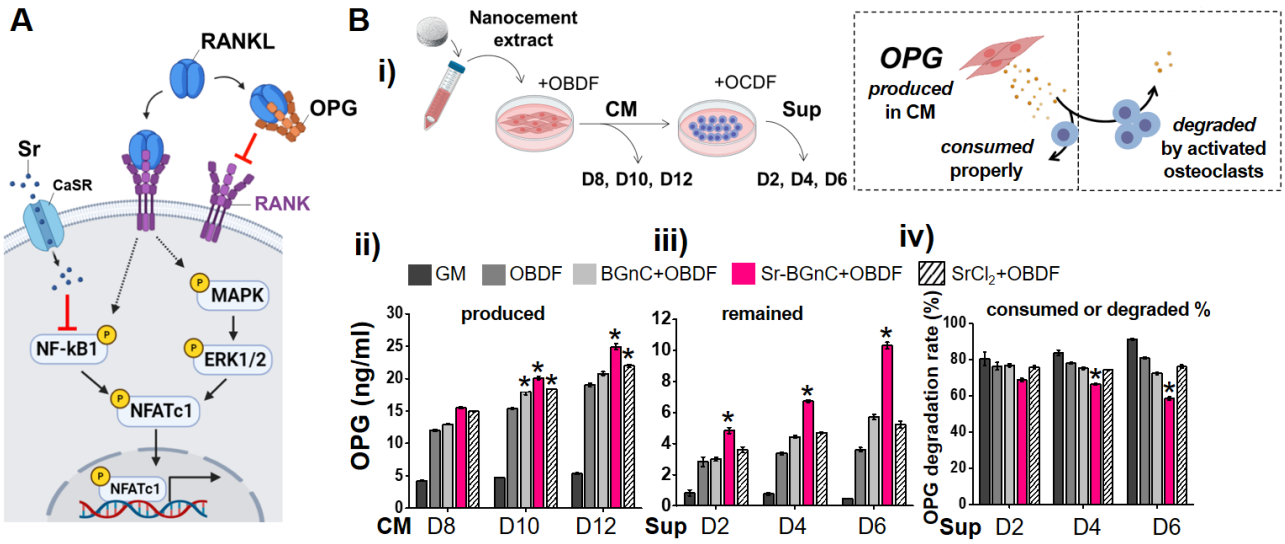

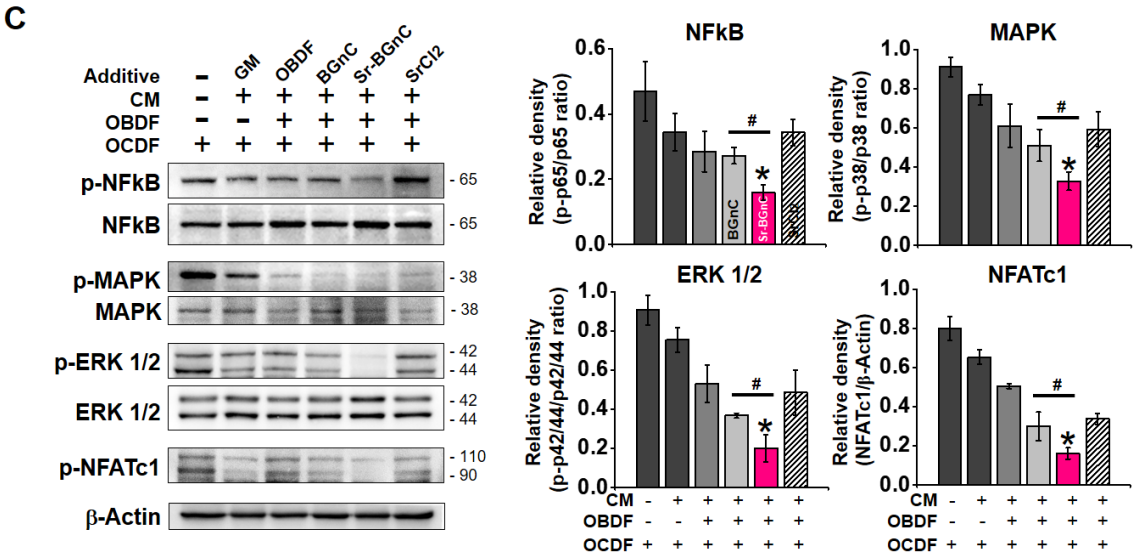

Figure 5. Osteoclastic inhibitory signaling by interplay of osteoblasts (secreted OPG) and osteoclasts through Sr-BGnC. (A) Schematic illustration showing the effects of Sr-BGnC (Sr ions) on the interplay of osteoblasts (secreted molecules) and osteoclasts (receptor), and the intracellular signaling pathways. Osteoblasts-conditioned media collected from the MC3T3-E1 cell culture with the nanocements were treated to RAW264.7 cells during the osteoclast differentiation. (B) Measurement of OPG; schematic diagram of the sampling for quantification, illustrating that the conditioned media were collected at day 8, 10 and 12 while the culture supernatant of RAW264.7 cells were collected at day 2, 4, and 6 of osteoclast differentiation, in which OPG was either consumed properly or degraded by osteoclasts when highly activated (i). ELISA results of OPG produced in the conditioned medium (ii) or consumed / degraded in the supernatant (iii), and the percentage of OPG consumed or degraded (iv) was calculated. (C) Intracellular signaling molecules involved in the osteoclastic inhibition, as analyzed by western blot. Band intensities were quantified and the phosphorylated ratios were presented. * indicates $p<0.05$ *versus* OBDF only group (n = 3), and $^{\#}$ indicates $p<0.05$ *versus* BGnC-OBDF group (n = 3).

2.5. Bone tissue regeneration in an ovariectomized rat model

The above results show that the Sr-BGnC possesses dual-capacity for promoting osteogenesis and inhibiting osteoclastogenesis, which is favorable for osteoporotic bone regeneration. To confirm the efficacy *in vivo* we modeled ovariectomized osteoporosis in rats. After 3 months of osteoporosis induction by ovariectomy, a burr hole defect was created in rat tibia, which was treated with the nanocement sample, as illustrated in **Fig. 6A**. After 8 weeks of implantation, tissue samples were evaluated by μCT and histological analyses. The μCT images of the sectioned tibia revealed the defect and surrounding bone tissue (**Fig. 6B**). The 3D constructed bone formation in the defect region was also enlarged. Based on the images, morphometric analyses of region of interest (ROI) were carried out to quantify the bone volume and mineral density. Results showed the nanocement groups significantly enhanced the bone volume but not the mineral density, and the enhancement was higher in Sr-BGnC than in BGnC group (**Fig. 6C**). The little difference in mineral density value among groups might be due to that the analyzed bone is cortical. However, the effect of Sr-BGnC on increasing bone volume in an osteoporotic tibia defect was explicit.

Next the bone area distanced (6 mm) from the defect (implanted area) in cortical bone was analyzed which might help understanding the possible effects of ions released from the nanocements. In particular, the trabecular bone near the tibia condyle was considered as ROI in which not only the bone quantity (volume) but the quality (bone density) can also be analyzed properly. The µCT images of the cross-sectional bone area revealed higher bone intensity in the nanocement groups (**Fig. 6D**). From a quantification, the bone volume and trabecular bone indices (trabecular number and thickness) were found to be significantly higher in the nanocement groups, particularly in Sr-BGnC while the trabecular spacing was decreased (**Fig. 6E**). This effect is possibly due to the therapeutic ions released from the nanocement as can be deduced from the results in the *in vitro* conditions (provided in Fig. 1Ciii & Table S1). However, the *in vivo* system is dynamic (time-dependent and interactive with many types of cells) and open, which is different from the *in vitro* acellular closed system, making it difficult to directly correlate the two systems. While the *in vivo* measurement of the local ionic concentrations remain challenging, the increased bone density by the nanocement around the area even away from the implanted site (6 mm distanced) is noteworthy, suggesting the role of *in vivo* local ions possibly released from the nanocement in promoting osteoporotic bone regeneration.

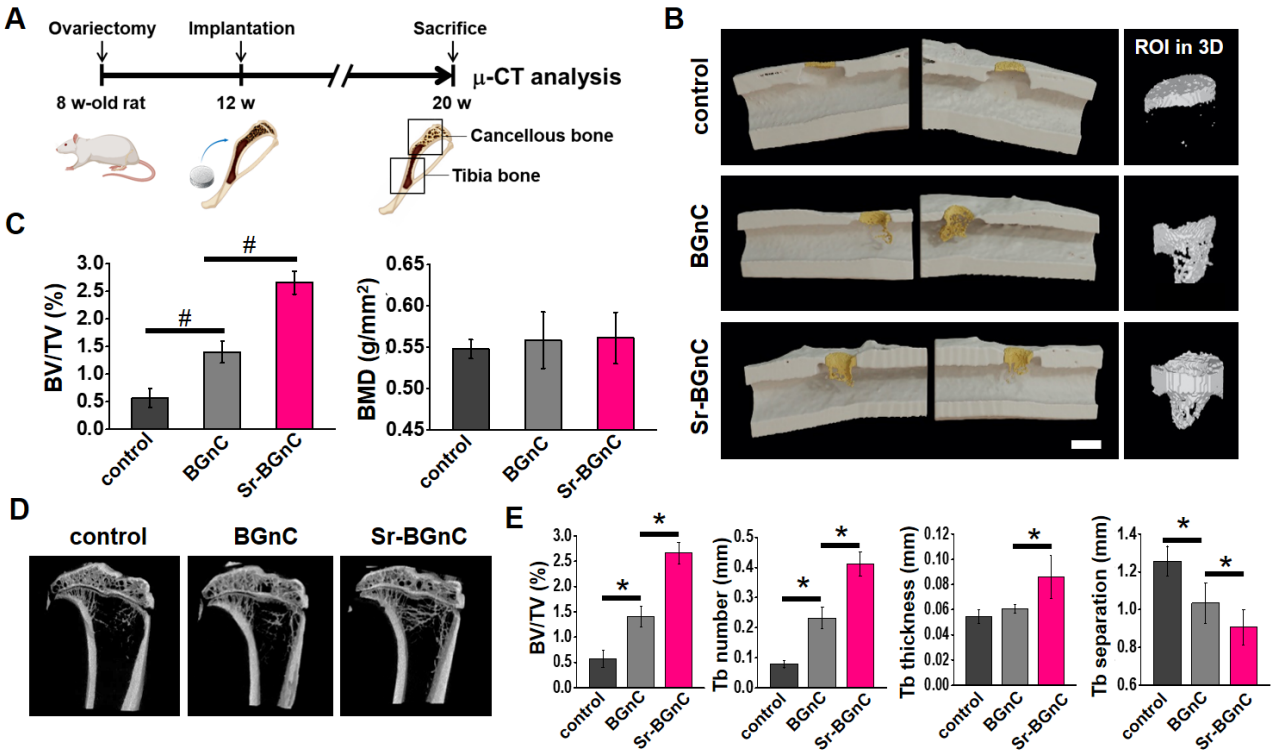

Figure 6. ***In vivo*** **osteoporotic bone regeneration by Sr-BGnC in an ovariectomized rat model.** (A) Schematic timeline for the *in vivo* study; a burr hole defect was created in rat tibia at 3-month post-induction of osteoporosis by ovariectomy, and the nanocement sample was implanted into the defect. After 8 weeks of implantation, the *in vivo* bone regeneration was evaluated by µCT and histology. (B,C) µCT analysis of cortical bone region; (B) µCT images showing neo-bone formation pseudo-colored in yellow according to the morphometric analysis (left, scale bar = 2 mm), and 3D reconstructed images of the neo-bone tissue (right), and (C) the quantitative analysis, showing the neo-bone volume (BV/TV) and bone mineral density (BMD). (D,E) µCT analysis of trabecular bone near the tibia condyle; (D) µCT images and (E) the quantitative analysis of the trabecular bone indices (bone volume, trabecular number, thickness and separation). * indicates $p<0.05$ between groups (n =5).

Next, the defect areas were analyzed by H&E, MT, and IHC staining to investigate the regenerative process at cell and molecular levels. As shown in **Fig. 7A**, new bone formation was pronounced in the nanocement groups, particularly in Sr-BGnC which contrasted with the defect control where new bone formation was minimal. Interestingly, an osteoinduction-like bone formation was noticed around the nanocement surface which also experienced substantial degradation. Tissue samples were further immunohistochemically stained for detection of bone-formation (BSP, OCN) and -resorption (RANKL) related proteins (**Fig. 7B**). The defect control group showed a strong RANKL (red color) expression, which however, was significantly weakened in nanocement groups (down to ~10-30% *w.r.t.* control), especially in Sr-BGnC. On the other hand, the expression of BSP and OCN (green color) was significantly higher in nanocement groups (~300-400% *w.r.t.* control), particularly in Sr-BGnC. A number of osteoblasts were found in the new bone surrounding area (red arrowheads, Figure.7C). Of note, the number of osteoblasts counted from the H&E stained images was significantly different; Sr-BGnC >> BGnC >> control (**Fig. 7C**). Taken together, the Sr-BGnC was highly effective in the osteoporotic bone regeneration through multiple (dual) actions, *i.e.*, increasing bone forming event while decreasing bone resorbing activity which ultimately resulted in overcoming the unbalanced bone remodeling process that otherwise would represent problematic osteoporotic symptoms.

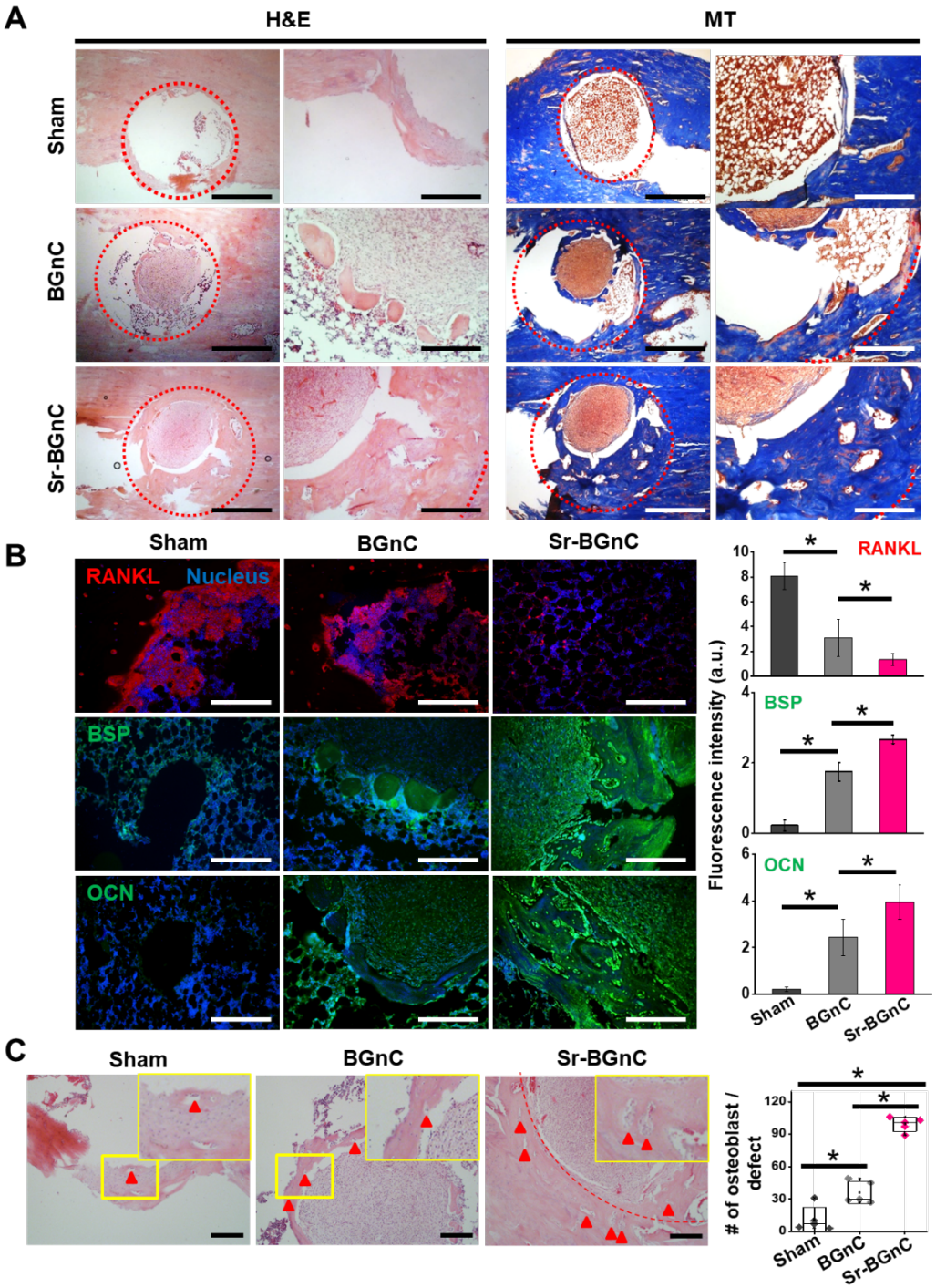

Figure 7. Histological evaluation of the *in vivo* osteoporotic bone defect regeneration by Sr-BGnC treatment. (A) H&E and (B) MT staining of the nanocements harvested with surrounding tissues at 8 weeks of post-implantation (scale bar = 1 mm and 200 μm for low and high magnification, respectively). The circle indicates the nanocement implant. (B) Immunohistochemical staining for bone resorption marker, RANKL (red) and bone formation markers, BSP and OCN (green) (scale bar = 200 μm). Tissues were counterstained with DAPI. Fluorescence intensity of each marker was quantitatively analyzed by Image J. (C) Analysis of the number of osteoblasts in the regenerated tissues. Red arrowheads indicate osteoblasts. The dotted line indicates boundary of the defect site (scale bar = 200 μm). * indicates $p<0.05$ between groups (n = 5).

While here we focused on the osteoblastic and osteoclastic activity of the nanocements in bone regeneration, other biological properties such as angiogenesis might also be of special importance [79, 80]. From an *in vitro* experiment of angiogenesis (supplementary data, **Fig. S7**), we observed that the Sr-BGnC induced tubule formation of endothelial cells (HUVECs) in a similar level to the Sr-free nanocement (BGnC), which is known to be pro-angiogenic due to the release of silicate ions; furthermore, the nanocement samples tested in a rat subcutaneous tissue up to 4 weeks (supplementary data, **Fig. S8**) demonstrated that the Sr-BGnC had a substantial pro-angiogenic activity that was comparable to the Sr-free nanocement (BGnC), suggesting that the Sr-BGnC could preserve the pro-angiogenic capacity of the Sr-free nanocement, which might also positively function in bone regeneration in the osteoporotic conditions which yet needs further in-depth evaluations.

3. Concluding remarks

The findings in this study are schematically summarized in **Fig. 8** that illustrates the multiple actions of the Sr-nanocement particularly mediated by the released ionic cues in terms of pro-osteogenesis and anti-osteoclastogenesis (primarily), and pro-angiogenesis (additionally), under the osteoporotic conditions. The Sr-BGnC releases triple ions (Sr, silicate, and Ca), among which those considered to be osteo-promotive (Sr, Ca) and pro-angiogenic (silicate) accelerate the bone forming process while those involved in osteoclastogenesis inhibition (Sr, silicate; either directly on osteoclasts or indirectly through osteoblasts) slow down the bone resorption events, which, collectively, coordinating balanced bone remodeling and regeneration, resolving the osteoporotic pathological conditions. In particular, the routes of osteoclastic inhibition actions of Sr-BGnC were not just directly on osteoclasts, but also through the stimulation of osteoblasts and their interplay with osteoclasts. The effectiveness of the Sr-BGnC in the osteoblasts/osteoclasts regulation was evidenced in an ovariectomized (osteoporotic) tibial defect model in rats over 8 weeks. While here we focused on the osteoclast/osteoblast interactions, there is growing evidence of the important roles of macrophages related with implanted biomaterials played in bone forming process [81-84] . Therefore, the interactions of macrophages with osteoblasts or osteogenic cells might be an important agenda that warrants further study. The examination of a secondary bone remodeling process following the healing step would also need to address the long-term effects of Sr-BGnC in osteoporotic bone. Lastly, the performance of the Sr-BGnC in large animal models is needed to find future clinical availability for the treatment of osteoporosis as therapeutic biomaterials. Along with the ionic actions, given the additional ability of the bioactive nanoglass to loading small molecules and proteins, the potential of the Sr-BGnC for bone therapeutics can be reinforced, which yet to be investigated in future studies.

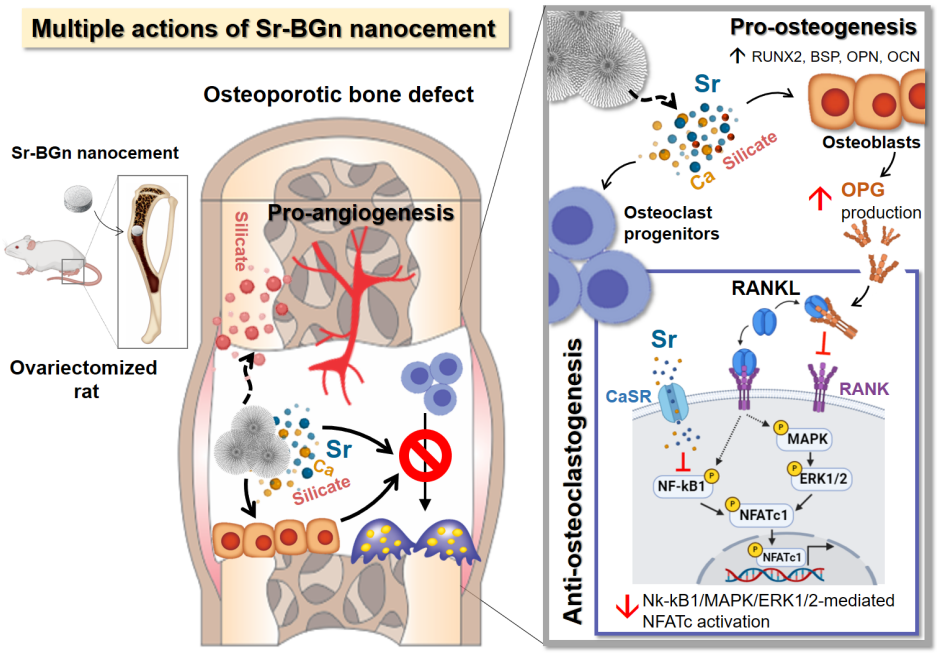

Figure. 8. Schematic summarizing the multiple-actions of Sr-BGnC in the regeneration of osteoporotic bone defect. The multiple actions of the Sr-nanocement particularly mediated by the released multiple ionic cues in terms of pro-osteogenesis and anti-osteoclastogenesis (primarily), and pro-angiogenesis (additionally), under the osteoporotic conditions. The Sr-BGnC releases triple ions (Sr, silicate, and Ca), among which those considered to be osteo-promotive (Sr, Ca) and pro-angiogenic (silicate) accelerate the bone forming process while those involved in osteoclastogenesis inhibition (Sr, silicate) slow down the bone resorption events, which, collectively, coordinating balanced bone remodeling and regeneration, resolving the osteoporotic pathological conditions. In particular, the routes of osteoclastic inhibition actions of Sr-BGnC were not just directly on osteoclasts, but also through the stimulation of osteoblasts and their interplay with osteoclasts. The effectiveness of the Sr-BGnC in the osteoblasts/osteoclasts regulation was evidenced in an ovariectomized (osteoporotic) tibial defect model in rats over 8 weeks.

4. MATERIALS AND METHODS

4.1. Materials

4.1.1. Preparation of nanoparticles (Sr-BGn) and nanocements (Sr-BGnC)

Large pore-sized BG nanoparticles incorporated with Sr ions (0 and 5% w/w) were produced by a sol-gel method using hexadecyltrimethylammonium bromide (CTAB, H5882, Sigma Aldrich, Darmstadt, German) as a structural template. In a typical synthesis, CTAB (1g), calcium nitrate tetrahydrate (C1396, Sigma Aldrich) (0.141g) and strontium nitrate (204498, Sigma Aldrich) (0.084g) were dissolved in a mixture of water, ethanol anhydrous (459836, Sigma Aldrich) and ethyl ether (60-29-7, Sigma Aldrich) (7: 1: 2 (v/v/v), 200ml). Tetraethyl orthosilicate (TEOS, 333859, Sigma Aldrich) (1.4g) solution was added dropwise into the mixture under stirring. After 4 h of reaction, white precipitate particles were collected and washed with deionized water and ethanol. Samples were dried at 60°C overnight and subsequently calcined at 550°C for 10 h to remove the

remaining CTAB and the organic template.

To form nanocement, Sr-BGn powder was mixed with 2.5wt% NaH_2PO_4 liquid at various powder/liquid ratios (P/L ratios) in the range of 0.3 to 0.5. The cement paste was placed in a cylindrical mold (6 mm diameter x 4 mm height), and then dried at 37°C with 100% humidity condition. BGn nanocement (BGnC) was also prepared by the same procedure as the Sr-BGnC preparation for comparison.

4.1.2. Characterizations of samples

The morphology and structure of the prepared nanocements were examined by using transmission electron microscopy (TEM, JEM-3010, JEOL Ltd, Tokyo, Japan). The atomic composition of samples was detected by energy dispersive spectroscopy (EDS, Oxford) attached to TEM. The phase of samples was confirmed by X-ray diffraction (XRD, Rigaku, Ultima IV, Japan) with Cu Ka radiation at 40 mA and 40 kV, at a step size of 0.02° and a scanning speed of 2.0°/min. The attenuated total reflectance–Fourier transform infrared spectroscopy (ATR–FTIR, Varian 640-IR) with a GladiATR diamond crystal accessory (026-2100, PIKE Technologies, Madision, USA) was used to examine the chemical bond structure. The zeta (ξ)-potential of the sample dispersed in DW was measured using a Laser Doppler electrophoresis (LDE) instrument (Zetasizer Nano ZS, Malvern, UK). The mesoporosity of the samples was characterized by N_2 adsorption/desorption isothermal process. The surface area and pore volume were calculated based on the Brunauer–Emmett–Teller (BET) method and the average pore size was calculated according to the Barrett–Joyner–Halenda (BJH) method.

4.1.3. Ionic release test

Ions release of Sr-BGnC was monitored at 37°C for 14 days. Each sample was prepared as a disc shape (6 mm in diameter x 4 mm in thickness). One disc-shaped sample was soaked in Tris–HCl buffer (10ml, pH 7.4) at 37 °C. The supernatant was collected at different time points and replaced with fresh buffer. Also, the ions released from both nanocements (BGnC, Sr-BGnC) in α-MEM were collected after 24 h of incubation at 37°C. The $SrCl_2$ 1 mM in α-MEM was used for a comparison group (free-Sr ions). The amount of ions released was measured by the inductively coupled plasma atomic emission spectrometry (ICP-AES, OPTIMA 4300 DV, Perkin-Elmer, USA). Three replicate samples were tested for each condition.

4.2. In vitro cell studies

The experimental details for the *in vitro* cell culture studies are summarized in Table 2.

4.2.1. Nanocement samples for in vitro cell studies

Sterilized nanocements (BGnC and Sr-BGnC) were incubated in 10 ml of α-MEM (SH30265.01, Hyclone, Utah, USA) containing 1% (v/v) penicillin-streptomycin (PS, 15140-122, Gibco, USA) at 37°C with a shaking speed of 120 rpm. After 24 h of extraction, the supernatant was collected by centrifugation at 3000 rpm for 5 min and then filtered through a 0.22 μm pore syringe filter. Prior to the cell culture, fetal bovine serum (FBS, 35-015-CV, Corning, Woodland, Ca) was added into the extracts at a concentration of 10% (v/v). In addition, α-MEM containing 1 mM $SrCl_2$ was prepared as a control.

4.2.2. Cells

In vitro studies of osteogenesis and osteoclastogenesis were evaluated with pre-osteoblast cell line MC3T3-E1 (ATCC, CRL-2593™) and pre-osteoclast cell line RAW 264.7 (ATCC, TIB-71™), respectively. Bone cell lines were obtained from the American type culture collection (ATCC, VA, USA). MC3T3-E1 cells were maintained in α-MEM without ascorbic acid (MEM- α, A1049001, Gibco, USA) including 10% (v/v) of FBS and 1% (v/v) PS under 5% CO_2 and humidified atmosphere of 37°C. MC3T3-E1 cells were plated at a density of 1 x 10^5 in each well of 6-well plates. For the osteogenic stimulation, at 24 h after plating, the culture medium was replaced by the nanocement extracts supplemented with osteogenic differentiation factors including 50 mg/ml L-ascorbic acid (11540, USB corporation, OH, USA), 10 mM β-glycerophosphate (G9422, Sigma Aldrich, USA) and 100 nM dexamethasone (Sigma Aldrich). The medium was changed every two days. After 6 days of osteogenic differentiation, the culture supernatants were collected every two days (from day 8 to day 12) for three times as conditioned media and subsequently treated to RAW264.7 cells. Prior to the treatment, the supernatants were centrifuged at 3000 rpm for 3 min to remove cell debris. RAW264.7 cells were cultured in Dulbeco's modified Eagle medium (DMEM, LM 001-05 Welgene, South Korea) including 10% (v/v) of FBS and 1% (v/v) PS under 5% CO_2 and humidified atmosphere of 37°C. Cells were seeded at a density of 1 x 10^5 in each well of 6-well plates. After 24 h, the culture medium was replaced by the culture supernatant from MC3T3-E1 cells. For the osteoclast differentiation, the culture supernatant was supplemented with 50 ng/ml of RANKL (310-01, Peprotech, NJ, USA), 10 ng/ml of M-CSF (315-02, Peprotech) and 1 ng/ml of TGF-β2 (7666-MB-005, R&D systems, MN, USA). The medium was changed every two days.

Rat bone marrow derived mesenchymal stem cells (rMSCs) were isolated for the osteogenic differentiation study. All protocols involving animals were approved by the Animal Care and Use Committee of Dankook University. In brief, 5 weeks of adult male Sprague-Dawley rats were sacrificed and the proximal and distal femora and tibia were cut off and then flushed out with PBS. The collected tissues were washed with complete cell culture medium for 5 times and placed in a culture dish under a humidified atmosphere of 5% CO_2 at 37°C. The cells at passage 3 were used for the study.

4.2.3. ALP and ARS staining

Alkaline phosphatase (ALP) and alizarin red S (ARS) staining was performed to detect the differentiation and

mineralization of MC3T3-E1 and rMSC, respectively. For the ALP staining, cells were washed with phosphate buffered saline (PBS) and fixed with 4% (v/v) paraformaldehyde for 30 min. After washing with PBS three times, cells were stained with an ALP stain solution (Sigma, FAST BCIP/NBT tablet) prepared according to the manufacturer's instructions. Briefly, one Sigma FAST BCIP/NBT tablet was dissolved in 10 ml DW and treated to the fixed cells for 1 h at 37°C incubator. The images were taken by a scanner (V300, EPSON BATAM, Indonesia) after washing with DW. For the ARS staining, cells were stained with an ARS solution (pH 4.2) at room temperature for 5 min. Cells were washed with DW five times and the images were taken by a scanner (V300, EPSON BATAM, Indonesia). The calcium deposits of the cells were dissolved in 10% (w/v) cetylpyridinium chloride (CPC, C0732, Sigma Aldrich, MO, USA) solution for 1 h at room temperature with shaking. The eluate was transferred to a 96-well plate and measured at 565 nm using a microplate reader (SpectraMax M2, Molecular device, USA).

4.2.4. Gene expressions by quantitative real time PCR

To evaluate the osteogenesis- and osteoclastogenesis-related gene expression, quantitative real-time polymerase chain reaction (qRT-PCR) was performed on cells. MC3T3-E1 cells were collected at day 3, 7, and 14 of culture in the osteogenic differentiation medium. The expression levels of osteogenesis-related genes including runt-related transcription factor 2 (*Runx2*), bone sialoprotein (*Bsp*), osteopontin (*Opn*) and osteocalcin (*Ocn*) were evaluated. The osteoclastogenesis-related gene expression was also investigated in RAW264.7 cells after 3 days of culture in the BGnC and Sr-BGnC extracts supplemented with osteoclast differentiation factors. The expression levels of osteoclastogenesis-related genes including calcium-sensing receptor (*Casr*), nuclear factor of activated T-cells-cytoplasmic 1 (*Nfatc-1*), Fos Proto-oncogene (*c-fos*), tartrate-resistant acid phosphatase type 5 (*Acp5*), cathepsin K (*Ctsk*), and matrix metalloproteinase-9 (*Mmp9*) were assessed. The qRT-PCR primers and their sequences are listed in Table 3.

After cells were collected, mRNA was isolated using Ribospin kit (GeneAll, 304-150, Seoul, Korea) according to the manufacturer's instructions. cDNA was subsequently synthesized using AccuPower PCR premix (Bioneer, K-2011, Deajeon, Korea) and the reverse transcription was performed using a thermal cycler (HID Veriti® 96-Well Thermal Cycler, 447907, Applied Biosystems, Singapore). For qRT-PCR, SensiMix™ SYBR Hi-ROX kit (Bioline, QT605-05) with additional $MgCl_2$ (BIO-37026, Bioline) was used and qRT-PCR performed by StepOne^{TM} Plus (Applied Biosystems). The fold change of the gene expression was calculated by comparative Ct method ($2^{-\Delta\Delta Ct}$) and normalized to an endogenous housekeeping gene, GAPDH.

4.2.5. TRAP staining and activity assay

The RAW 264.7 cells were cultured in complete α-MEM or in osteoblast-conditioned medium in the presence of osteoclast differentiation factors for 6 days and were harvested for the further studies. After 6 days of culture, cells were fixed with 10% (v/v) of formalin neutral buffer solution (Tech & Innovation) for 30 min at room

temperature and stained with TRAP solution (MK300, TAKARA biomedical, Japan) for 30 min at 37°C. To stop the extra staining, cells were washed with DW and analyzed under a light microscope (IX71, Olympus, Tokyo, Japan). The TRAP activity was measured using TRAP assay kit (MK301, TAKARA biomedical, Japan) according to the manufacturer's instructions.

4.2.6. Pit formation assay

The bone resorption activity of differentiated RAW264.7 cells were evaluated by a pit formation assay. RAW264.7 cells were seeded at a density of $2x10^4$ cells per well of Osteo Assay Plate (CLS3987, Corning, ME, USA). The osteoclast maturation of RAW264.7 cells was induced by the culture supernatant of MC3T3-E1 cells supplemented with osteoclast differentiation factors. After 6 days of the induction, cells were removed by treating 5% (v/v) bleach and imaged by an optical microscope. The pit area was quantified by ImageJ software (National Institutes of Health, Bethesda, MD, USA).

4.2.7. Western blot

For total protein extraction, RAW264.7 cells were lysed in RIPA lysis buffer (EBA-1149, ELPIS biotech, Korea) containing protease inhibitor (Halt™ Protease and Phosphatase Inhibitor Cocktail (100X), 78440, Thermo Scientific, USA). The total protein concentration was quantified using a Pierce BCA protein assay kit (23225, Thermo scientific). An equal amount of total proteins per lane was electrophoresed in polyacrylamide gels and transferred onto polyvinylidene difluoride (PVDF) membranes. The membranes were blocked with 5% (w/v) skim milk (BD Biosciences, Sparks, MD, USA) in TBST solution for 1 h, and then incubated with primary antibodies in 1% (w/v) skim milk in TBST solution at 4°C overnight against NFκB (nuclear factor kappa-light-chain-enhancer of activated B cells), MAPK (mitogen-activated protein kinase), ERK 1/2 (Extracellular signal-regulated kinases), NFATc1, or β-actin. After washing with TBS-T (Tris-Buffered Saline-0.1% Tween), the membranes were further incubated with secondary antibodies at room temperature for 1 h. The signals were detected using Western Blot Imaging system (ibright FL1500, Invitrogen, Singapore) and the band intensity was normalized with β-actin and quantified by ImageJ.

4.2.8. Evaluation of transcriptional activity by luciferase reporter assay

Transcriptional activity of 6XOSE and OG2 was measured using luciferase reporter assay. MC3T3-E1 cells ($1x10^6$ per well of 6-well plates) were cultured for 5 days and transfected with luciferase reporter gene plasmids using CalFectin mammalian Cell Transfection Reagent (SL100478, Signagen, USA). The nanocement extracts were treated to cells after 24 h of transfection and the luciferase activity was detected after 3 days of additional culture.

RAW264.7 ($1x10^6$) cells were transfected with NFATc1 luciferase reporter gene plasmids using Lipofectamine™ 3000 Transfection Reagent (L3000008, Life technologies, California, USA). Renilla, a

luciferase control reporter vector (E2231, pRLTK, Promega) plasmids, was used as a normalization control to confirm the transfection efficiency. After 24 h of transfection, cells were harvested and seeded at a density of $1x10^5$ cells per well of 6-well plates. On the next day, cells were treated with BGnC or Sr-BGnC extracts supplemented with osteoclast differentiation factors for 48 h. The luciferase activity was evaluated by Dual glow luciferase assay (E2920, Promega, MA, USA) and the luminescence was measured using a microplate reader (Varioskan LUX, Thermofisher Scientific, Singapore).

4.2.9. ELISA for OPG and RANKL

The culture supernatants collected from MC3T3-E1 and RAW246.7 cells undergoing the differentiation were collected respectively and the amount of OPG (ab100733) and RANKL (ab100749, Abcam, MA, USA) in the supernatants of pre-osteoblast cells and pre-osteoclast cells were quantified by sandwich ELISA as manufacturer's protocol. All the supernatants were centrifuged at 1500 rpm for 10 min to remove cell debris before the assay. Absorbance was measured at 450 nm using microplate reader (iMark, Biorad, USA) and the OD value was converted based on a standard curve. Data was obtained from two independent biological replicates (n = 3 each time).

4.3. In vivo animal studies

4.3.1. Tissue compatibility in subcutaneous tissue

Tissue compatibility of the nanocements was evaluated in the subcutaneous tissue of 10-week-old male Sprague-Dawley rats. The animal protocol was approved by the Institutional Animal Care and Use Committee (IACUC) in Dankook University. Briefly, the nanocements were sterilized with ethylene oxide gas treatment prior to implantation. The surgery was performed under general anesthesia with an intramuscular injection of ketamine (80 mg/kg) and xylazine (10 mg/kg). The operatory region of dorsal skin was shaved and achieved asepsis condition by applying povidone and ethanol. A subcutaneous pocket was made followed by a long linear incision and one cement was inserted into the pocket. Four of the nanocements (6 mm in diameter x 4 mm in height) were implanted in each rat and the group was randomly allocated. The incision was sutured after the implantation with 4-0 non-absorbable mono-filament suture material (Prolene, Braun, Germany). The animals were sacrificed after 2 and 4 weeks of surgery and the implanted samples were collected with the surrounding tissues for histology. The collected samples were fixed in 10 % (v/v) neutral buffered formalin (NBF) and dehydrated in a series of graded ethanol. The samples were bisected and embedded in paraffin. The paraffin blocks were sectioned with a microtome (Leica RM2255, USA) in 5-μm thickness, and then 4 sections were randomly selected for the staining with hematoxylin and eosin (H&E) or Masson's trichrome (MT). The images of the stained samples were taken by a light microscope and the new blood vessel formation of the tissue was analyzed by Image J.

4.3.2. Ovariectomized osteoporotic bone defect model

The nanocements were implanted in tibia defects of an ovariectomy-induced osteoporotic defect model in rats. A total of nine ovariectomized rats and both legs were used for the implantation. The implants were randomly assigned as intact (n=3), Sham control (n=5), BGnC (n=5), or Sr-BGnC (n=5) group. After 12 weeks of ovariectomy, the animals were anesthetized with ketamine (80 mg/kg) and xylazine (10 mg/kg) through intraperitoneal injection for following burr-hole defect operation. Each hindlimb was shaved and sterilized with 70% ethanol. A 2 cm of longitudinal incision was made on the anteromedial side of the tibia, and the tibialis anterior muscle was bluntly dissected. The cylindrical defect (2 mm in diameter x 2 mm in depth) was made on the middle of the anteromedial side (10 mm away from the growth plate, equal to 6 mm from the trabecular bone) using a low-speed round diamond burr under continuous saline irrigation. Each nanocement (2 mm diameter x 2 mm height) was placed in the defect and the muscle incision was sutured by the simple interrupted suture with 4-0 Dafilon®.

4.3.3. In vivo tissue sample analyses

The animals were sacrificed at 8 weeks post-operation, and μCT analysis was performed to visualize the hard tissue formation [85]. The defect was visualized using a μCT scanner (SkyScan, Belgium) with a camera pixel size of 12.56 mm/1 mm aluminum. The collected tissue samples were fixed in 4% (v/v) neutral buffered formalin and subsequently decalcified in fast decalcified solution, followed by embedding in paraffin.

For histological analysis, tissue slices (5 μm thickness) were stained with H&E and MT. For immunohistochemical (IHC) staining, the tissue slides were incubated with primary antibodies against RANKL (1:200), BSP (1:200), OCN (1:200) at 4°C overnight, followed by treatment of Alexa Flour® 594 or 488-conjugated secondary antibodies at room temperature for 1 h. Nuclei were counterstained with DAPI (P36935, Invitrogen). Images were taken with a microscope (IX71, Olympus, Japan) and the fluorescence intensity was quantified by ImageJ.

4.4. Statistics

Data are presented as the mean ± one standard deviation. Comparisons among groups were carried out using one-way analysis of variance (ANOVA) with Bonferroni post hoc test. Statistical significance was considered at $*p < 0.05$ and $**p < 0.01$.

Supporting Information

Figure S1~S8

Table S1~S2

Conflict of Interest: All authors declare no conflict of interest.

Acknowledgments: This work was supported by the grants (2019R1C1C1002490, 2018R1A2B3003446, 2018K1A4A3A01064257, 2019R1A6A1A11034536, 2015K1A1A2032163, 2021R1A5A2022318), National Research Foundation, Republic of Korea.

Data availability: The raw/processed data required to reproduce these findings cannot be shared at this time due to technical or time limitations. However, they can be provided upon requested.

References

[1] Yadav VK, Balaji S, Suresh PS, Liu XS, Lu X, Li Z, et al. Pharmacological inhibition of gut-derived serotonin synthesis is a potential bone anabolic treatment for osteoporosis. Nat Med. 2010;16:308-12.

[2] Peacock M. Calcium metabolism in health and disease. Clin J Am Soc Nephrol. 2010;5 Suppl 1:S23-30.

[3] Banerjee I, Zhang J, Moore-Morris T, Pfeiffer E, Buchholz KS, Liu A, et al. Targeted Ablation of Nesprin 1 and Nesprin 2 from Murine Myocardium Results in Cardiomyopathy, Altered Nuclear Morphology and Inhibition of the Biomechanical Gene Response. PLoS Genet. 2014;10:e1004114.

[4] Black DM, Rosen CJ. Clinical Practice. Postmenopausal Osteoporosis. N Engl J Med. 2016;374:254-62.

[5] Khosla S, Amin S, Orwoll E. Osteoporosis in men. Endocr Rev. 2008;29:441-64.

[6] Shuid AN, Khaithir TMN, Mokhtar SA, Mohamed IN. A systematic review of the outcomes of osteoporotic fracture patients after hospital discharge: morbidity, subsequent fractures, and mortality. Ther Clin Risk Manag. 2014:937.

[7] Weycker D, Li X, Barron R, Bornheimer R, Chandler D. Hospitalizations for osteoporosis-related fractures: Economic costs and clinical outcomes. Bone Rep. 2016;5:186-91.

[8] Lavet C, Mabilleau G, Chappard D, Rizzoli R, Ammann P. Strontium ranelate stimulates trabecular bone formation in a rat tibial bone defect healing process. Osteoporos Int. 2017;28:3475-87.

[9] Johnell O, Kanis JA. An estimate of the worldwide prevalence and disability associated with osteoporotic fractures. Osteoporos Int. 2006;17:1726-33.

[10] Jobke B, Milovanovic P, Amling M, Busse B. Bisphosphonate-osteoclasts: changes in osteoclast morphology and function induced by antiresorptive nitrogen-containing bisphosphonate treatment in osteoporosis patients. Bone. 2014;59:37-43.

[11] Zhu S, Hu X, Tao Y, Ping Z, Wang L, Shi J, et al. Strontium inhibits titanium particle-induced osteoclast activation and chronic inflammation via suppression of NF-kappaB pathway. Sci Rep. 2016;6:36251.

[12] Cheng TL, Murphy CM, Ravarian R, Dehghani F, Little DG, Schindeler A. Bisphosphonate-adsorbed ceramic nanoparticles increase bone formation in an injectable carrier for bone tissue engineering. J Tissue Eng. 2015;6:2041731415609448.

[13] Forte L, Sarda S, Torricelli P, Combes C, Brouillet F, Marsan O, et al. Multifunctionalization Modulates Hydroxyapatite Surface Interaction with Bisphosphonate: Antiosteoporotic and Antioxidative Stress Materials. ACS Biomaterials Science & Engineering. 2019;5:3429-39.

[14] Kates SL, Ackert-Bicknell CL. How do bisphosphonates affect fracture healing? Injury. 2016;47 Suppl 1:S65-S8.

[15] Li M, Wan P, Wang W, Yang K, Zhang Y, Han Y. Regulation of osteogenesis and osteoclastogenesis by zoledronic acid loaded on biodegradable magnesium-strontium alloy. Sci Rep. 2019;9:933.

[16] Nishiguchi A, Taguchi T. Osteoclast-Responsive, Injectable Bone of Bisphosphonated-Nanocellulose that Regulates Osteoclast/Osteoblast Activity for Bone Regeneration. Biomacromolecules. 2019;20:1385-93.

[17] Ray S, Thormann U, Eichelroth M, Budak M, Biehl C, Rupp M, et al. Strontium and bisphosphonate coated iron foam scaffolds for osteoporotic fracture defect healing. Biomaterials. 2018;157:1-16.

[18] Rizzoli R, Laroche M, Krieg MA, Frieling I, Thomas T, Delmas P, et al. Strontium ranelate and alendronate have differing effects on distal tibia bone microstructure in women with osteoporosis. Rheumatol Int. 2010;30:1341-8.

[19] Rama R, Rout A, Venkatesan K, Antony M. Effect of alkyl chain length of tri-n-alkyl phosphate extractants on the electrochemical behaviour of U (VI) in ionic liquid medium. J Electroanal Chem.

2016;771:87-93.

[20] Hodsman AB, Bauer DC, Dempster DW, Dian L, Hanley DA, Harris ST, et al. Parathyroid hormone and teriparatide for the treatment of osteoporosis: a review of the evidence and suggested guidelines for its use. Endocr Rev. 2005;26:688-703.

[21] Bonnelye E, Chabadel A, Saltel F, Jurdic P. Dual effect of strontium ranelate: stimulation of osteoblast differentiation and inhibition of osteoclast formation and resorption in vitro. Bone. 2008;42:129-38.

[22] Gentleman E, Fredholm YC, Jell G, Lotfibakhshaiesh N, O'Donnell MD, Hill RG, et al. The effects of strontium-substituted bioactive glasses on osteoblasts and osteoclasts in vitro. Biomaterials. 2010;31:3949-56.

[23] Sadegh AB. Strontium Ranelate Using for the Treatment of Postmenopausal Osteoporosis. Biomedical Journal of Scientific & Technical Research. 2018;5.

[24] Hegde V, Jo JE, Andreopoulou P, Lane JM. Effect of osteoporosis medications on fracture healing. Osteoporos Int. 2016;27:861-71.

[25] O'Donnell S, Cranney A, Wells GA, Adachi JD, Reginster JY. Strontium ranelate for preventing and treating postmenopausal osteoporosis. Cochrane Database Syst Rev. 2006.

[26] Caverzasio J. Strontium ranelate promotes osteoblastic cell replication through at least two different mechanisms. Bone. 2008;42:1131-6.

[27] Marie PJ. Strontium ranelate: New insights into its dual mode of action. Bone. 2007;40:S5-S8.

[28] Marie PJ. Strontium ranelate: a physiological approach for optimizing bone formation and resorption. Bone. 2006;38:S10-4.

[29] Marie PJ. Strontium ranelate: a novel mode of action optimizing bone formation and resorption. Osteoporos Int. 2005;16 Suppl 1:S7-10.

[30] Reginster J-Y. Cardiac concerns associated with strontium ranelate. Expert Opin Drug Saf. 2014;13:1209-13.

[31] Pilmane M, Salma-Ancane K, Loca D, Locs J, Berzina-Cimdina L. Strontium and strontium ranelate: Historical review of some of their functions. Materials Science and Engineering: C. 2017;78:1222-30.

[32] Ge C, Chen F, Mao L, Liang Q, Su Y, Liu C. Strontium ranelate-loaded POFC/β-TCP porous scaffolds for osteoporotic bone repair. RSC Adv. 2020;10:9016-25.

[33] Li D, Chen K, Duan L, Fu T, Li J, Mu Z, et al. Strontium Ranelate Incorporated Enzyme-Cross-Linked Gelatin Nanoparticle/Silk Fibroin Aerogel for Osteogenesis in OVX-Induced Osteoporosis. ACS Biomaterials Science & Engineering. 2019;5:1440-51.

[34] Mao L, Xia L, Chang J, Liu J, Jiang L, Wu C, et al. The synergistic effects of Sr and Si bioactive ions on osteogenesis, osteoclastogenesis and angiogenesis for osteoporotic bone regeneration. Acta Biomater. 2017;61:217-32.

[35] Zhang Y, Wei L, Chang J, Miron RJ, Shi B, Yi S, et al. Strontium-incorporated mesoporous bioactive glass scaffolds stimulating in vitro proliferation and differentiation of bone marrow stromal cells and in vivo regeneration of osteoporotic bone defects. J Mater Chem B. 2013;1:5711-22.

[36] Zeng J, Guo J, Sun Z, Deng F, Ning C, Xie Y. Osteoblastic and anti-osteoclastic activities of strontium-substituted silicocarnotite ceramics: In vitro and in vivo studies. Bioact Mater. 2020;5:435-46.

[37] Lee JH, Mandakhbayar N, El-Fiqi A, Kim HW. Intracellular co-delivery of Sr ion and phenamil drug through mesoporous bioglass nanocarriers synergizes BMP signaling and tissue mineralization. Acta Biomater. 2017;60:93-108.

[38] Frasnelli M, Cristofaro F, Sglavo VM, Dirè S, Callone E, Ceccato R, et al. Synthesis and characterization of strontium-substituted hydroxyapatite nanoparticles for bone regeneration. Materials Science and Engineering: C. 2017;71:653-62.

[39] Naruphontjirakul P, Tsigkou O, Li S, Porter AE, Jones JR. Human mesenchymal stem cells differentiate into an osteogenic lineage in presence of strontium containing bioactive glass

nanoparticles. Acta Biomater. 2019;90:373-92.

[40] Zhang W, Zhao F, Huang D, Fu X, Li X, Chen X. Strontium-Substituted Submicrometer Bioactive Glasses Modulate Macrophage Responses for Improved Bone Regeneration. ACS Appl Mater Interfaces. 2016;8:30747-58.

[41] Weng L, Boda SK, Teusink MJ, Shuler FD, Li X, Xie J. Binary Doping of Strontium and Copper Enhancing Osteogenesis and Angiogenesis of Bioactive Glass Nanofibers while Suppressing Osteoclast Activity. ACS Appl Mater Interfaces. 2017;9:24484-96.

[42] Kargozar S, Montazerian M, Fiume E, Baino F. Multiple and Promising Applications of Strontium (Sr)-Containing Bioactive Glasses in Bone Tissue Engineering. Front Bioeng Biotechnol. 2019;7:161.

[43] Rohnke M, Pfitzenreuter S, Mogwitz B, Henß A, Thomas J, Bieberstein D, et al. Strontium release from Sr(2+)-loaded bone cements and dispersion in healthy and osteoporotic rat bone. Journal of controlled release : official journal of the Controlled Release Society. 2017;262:159-69.

[44] Lode A, Heiss C, Knapp G, Thomas J, Nies B, Gelinsky M, et al. Strontium-modified premixed calcium phosphate cements for the therapy of osteoporotic bone defects. Acta Biomater. 2018;65:475-85.

[45] Kang MS, Lee NH, Singh RK, Mandakhbayar N, Perez RA, Lee JH, et al. Nanocements produced from mesoporous bioactive glass nanoparticles. Biomaterials. 2018;162:183-99.

[46] Seo JJ, Mandakhbayar N, Kang MS, Yoon JY, Lee NH, Ahn J, et al. Antibacterial, proangiogenic, and osteopromotive nanoglass paste coordinates regenerative process following bacterial infection in hard tissue. Biomaterials. 2021;268:120593.

[47] Beck GR, Jr., Ha SW, Camalier CE, Yamaguchi M, Li Y, Lee JK, et al. Bioactive silica-based nanoparticles stimulate bone-forming osteoblasts, suppress bone-resorbing osteoclasts, and enhance bone mineral density in vivo. Nanomedicine. 2012;8:793-803.

[48] Wu C, Chen Z, Yi D, Chang J, Xiao Y. Multidirectional effects of Sr-, Mg-, and Si-containing

bioceramic coatings with high bonding strength on inflammation, osteoclastogenesis, and osteogenesis. ACS Appl Mater Interfaces. 2014;6:4264-76.

[49] Schuhladen K, Roether JA, Boccaccini AR. Bioactive glasses meet phytotherapeutics: The potential of natural herbal medicines to extend the functionality of bioactive glasses. Biomaterials. 2019;217:119288.

[50] Zhao F, Lei B, Li X, Mo Y, Wang R, Chen D, et al. Promoting in vivo early angiogenesis with sub-micrometer strontium-contained bioactive microspheres through modulating macrophage phenotypes. Biomaterials. 2018;178:36-47.

[51] Islam MT, Felfel RM, Abou Neel EA, Grant DM, Ahmed I, Hossain KMZ. Bioactive calcium phosphate-based glasses and ceramics and their biomedical applications: A review. J Tissue Eng. 2017;8:2041731417719170.

[52] Sabareeswaran A, Basu B, Shenoy SJ, Jaffer Z, Saha N, Stamboulis A. Early osseointegration of a strontium containing glass ceramic in a rabbit model. Biomaterials. 2013;34:9278-86.

[53] Thormann U, Ray S, Sommer U, Elkhassawna T, Rehling T, Hundgeburth M, et al. Bone formation induced by strontium modified calcium phosphate cement in critical-size metaphyseal fracture defects in ovariectomized rats. Biomaterials. 2013;34:8589-98.

[54] Totaro A, Panciera T, Piccolo S. YAP/TAZ upstream signals and downstream responses. Nat Cell Biol. 2018;20:888-99.

[55] Bruckner R, Tylkowski M, Hupa L, Brauer DS. Controlling the ion release from mixed alkali bioactive glasses by varying modifier ionic radii and molar volume. Journal of materials chemistry B. 2016;4:3121-34.

[56] Mneimne M, Hill RG, Bushby AJ, Brauer DS. High phosphate content significantly increases apatite formation of fluoride-containing bioactive glasses. Acta Biomater. 2011;7:1827-34.

[57] Lee MN, Hwang H-S, Oh S-H, Roshanzadeh A, Kim J-W, Song JH, et al. Elevated extracellular calcium ions promote proliferation and migration of mesenchymal stem cells via increasing

osteopontin expression. Exp Mol Med. 2018;50:1-16.

[58] Boldbaatar K, Dashnyam K, Knowles JC, Lee H-H, Lee J-H, Kim H-W. Dual-ion delivery for synergistic angiogenesis and bactericidal capacity with silica-based microsphere. Acta Biomater. 2019;83:322-33.

[59] Dashnyam K, Jin G-Z, Kim J-H, Perez R, Jang J-H, Kim H-W. Promoting angiogenesis with mesoporous microcarriers through a synergistic action of delivered silicon ion and VEGF. Biomaterials. 2017;116:145-57.

[60] Yoon H, Kim H-L, Chun Y-S, Shin DH, Lee K-H, Shin CS, et al. NAA10 controls osteoblast differentiation and bone formation as a feedback regulator of Runx2. Nat Commun. 2014;5:5176.

[61] Baek S, Singh RK, Khanal D, Patel KD, Lee E-J, Leong KW, et al. Smart multifunctional drug delivery towards anticancer therapy harmonized in mesoporous nanoparticles. Nanoscale. 2015;7:14191-216.

[62] Park KH, Park B, Yoon DS, Kwon S-H, Shin DM, Lee JW, et al. Zinc inhibits osteoclast differentiation by suppression of Ca2+-Calcineurin-NFATc1 signaling pathway. Cell Communication and Signaling. 2013;11:74.

[63] Huang YZ, Wu CG, Xie HQ, Li ZY, Silini A, Parolini O, et al. Strontium Promotes the Proliferation and Osteogenic Differentiation of Human Placental Decidual Basalis- and Bone Marrow-Derived MSCs in a Dose-Dependent Manner. Stem Cells Int. 2019;2019:4242178.

[64] Pemmer B, Hofstaetter JG, Meirer F, Smolek S, Wobrauschek P, Simon R, et al. Increased strontium uptake in trabecular bone of ovariectomized calcium-deficient rats treated with strontium ranelate or strontium chloride. J Synchrotron Radiat. 2011;18:835-41.

[65] Xing M, Wang X, Wang E, Gao L, Chang J. Bone tissue engineering strategy based on the synergistic effects of silicon and strontium ions. Acta Biomater. 2018;72:381-95.

[66] Yang F, Yang D, Tu J, Zheng Q, Cai L, Wang L. Strontium Enhances Osteogenic Differentiation of Mesenchymal Stem Cells and In Vivo Bone Formation by Activating Wnt/Catenin Signaling. Stem

Cells. 2011;29:981-91.

[67] Oryan A, Baghaban Eslaminejad M, Kamali A, Hosseini S, Sayahpour FA, Baharvand H. Synergistic effect of strontium, bioactive glass and nano-hydroxyapatite promotes bone regeneration of critical-sized radial bone defects. Journal of Biomedical Materials Research Part B: Applied Biomaterials. 2019;107:50-64.

[68] Cui X, Zhang Y, Wang J, Huang C, Wang Y, Yang H, et al. Strontium modulates osteogenic activity of bone cement composed of bioactive borosilicate glass particles by activating Wnt/β-catenin signaling pathway. Bioact Mater. 2020;5:334-47.

[69] Hyun J, Park J, Wang S, Kim J, Lee HH, Seo YS, et al. MicroRNA Expression Profiling in CCl(4)-Induced Liver Fibrosis of Mus musculus. Int J Mol Sci. 2016;17.

[70] Jia X, Long Q, Miron RJ, Yin C, Wei Y, Zhang Y, et al. Setd2 is associated with strontium-induced bone regeneration. Acta Biomater. 2017;53:495-505.

[71] Schröder HC, Wang XH, Wiens M, Diehl-Seifert B, Kropf K, Schloßmacher U, et al. Silicate modulates the cross-talk between osteoblasts (SaOS-2) and osteoclasts (RAW 264.7 cells): Inhibition of osteoclast growth and differentiation. J Cell Biochem. 2012;113:3197-206.

[72] Ochiai N, Nakachi Y, Yokoo T, Ichihara T, Eriksson T, Yonemoto Y, et al. Murine osteoclasts secrete serine protease HtrA1 capable of degrading osteoprotegerin in the bone microenvironment. Commun Biol. 2019;2:86.

[73] Peng S, Liu XS, Huang S, Li Z, Pan H, Zhen W, et al. The cross-talk between osteoclasts and osteoblasts in response to strontium treatment: involvement of osteoprotegerin. Bone. 2011;49:1290-8.

[74] Rochette L, Meloux A, Rigal E, Zeller M, Cottin Y, Vergely C. The Role of Osteoprotegerin and Its Ligands in Vascular Function. Int J Mol Sci. 2019;20.

[75] Boyce BF, Xing L. Functions of RANKL/RANK/OPG in bone modeling and remodeling. Archives of biochemistry and biophysics. 2008;473:139-46.

[76] Ikeda F NR, Matsubara T, Tanaka S, Inoue J, Reddy SV, Hata K, Yamashita K, Hiraga T, Watanabe T, Kukita T, Yoshioka K, Rao A and Yoneda T. Critical roles of c-Jun signalling in regulation of NFAT family and RANKL-regulated osteoclast differentiation. Journal of Clinical Investigation. 2006;114:475–84.

[77] Huang H, Ryu J, Ha J, Chang EJ, Kim HJ, Kim HM, et al. Osteoclast differentiation requires TAK1 and MKK6 for NFATc1 induction and NF-kappaB transactivation by RANKL. Cell death and differentiation. 2006;13:1879-91.

[78] Fu Y, Gu J, Wang Y, Yuan Y, Liu X, Bian J, et al. Involvement of the mitogenactivated protein kinase signaling pathway in osteoprotegerininduced inhibition of osteoclast differentiation and maturation. Mol Med Rep. 2015;12:6939-45.

[79] Peticone C, Thompson DS, Dimov N, Jevans B, Glass N, Micheletti M, et al. Characterisation of osteogenic and vascular responses of hMSCs to Ti-Co doped phosphate glass microspheres using a microfluidic perfusion platform. Journal of tissue engineering. 2020;11:2041731420954712.

[80] Lee JH PP, Jin GZ, Knowles JC, Kim HW. Materials roles for promoting angiogenesis in tissue regeneration. Progress in Materials Science. 2021.

[81] Yang A, Lu Y, Xing J, Li Z, Yin X, Dou C, et al. IL-8 Enhances Therapeutic Effects of BMSCs on Bone Regeneration via CXCR2-Mediated PI3k/Akt Signaling Pathway. Cell Physiol Biochem. 2018;48:361-70.

[82] Xie Y, Hu C, Feng Y, Li D, Ai T, Huang Y, et al. Osteoimmunomodulatory effects of biomaterial modification strategies on macrophage polarization and bone regeneration. Regen Biomater. 2020;7:233-45.

[83] Niu Y, Wang Z, Shi Y, Dong L, Wang C. Modulating macrophage activities to promote endogenous bone regeneration: Biological mechanisms and engineering approaches. Bioact Mater. 2021;6:244-61.

[84] Chen Z, Klein T, Murray RZ, Crawford R, Chang J, Wu C, et al. Osteoimmunomodulation for

the development of advanced bone biomaterials. Materials Today. 2016;19:304-21.

[85] Fragogeorgi EA, Rouchota M, Georgiou M, Velez M, Bouziotis P, Loudos G. In vivo imaging techniques for bone tissue engineering. Journal of tissue engineering. 2019;10:2041731419854586.

Supplementary Data

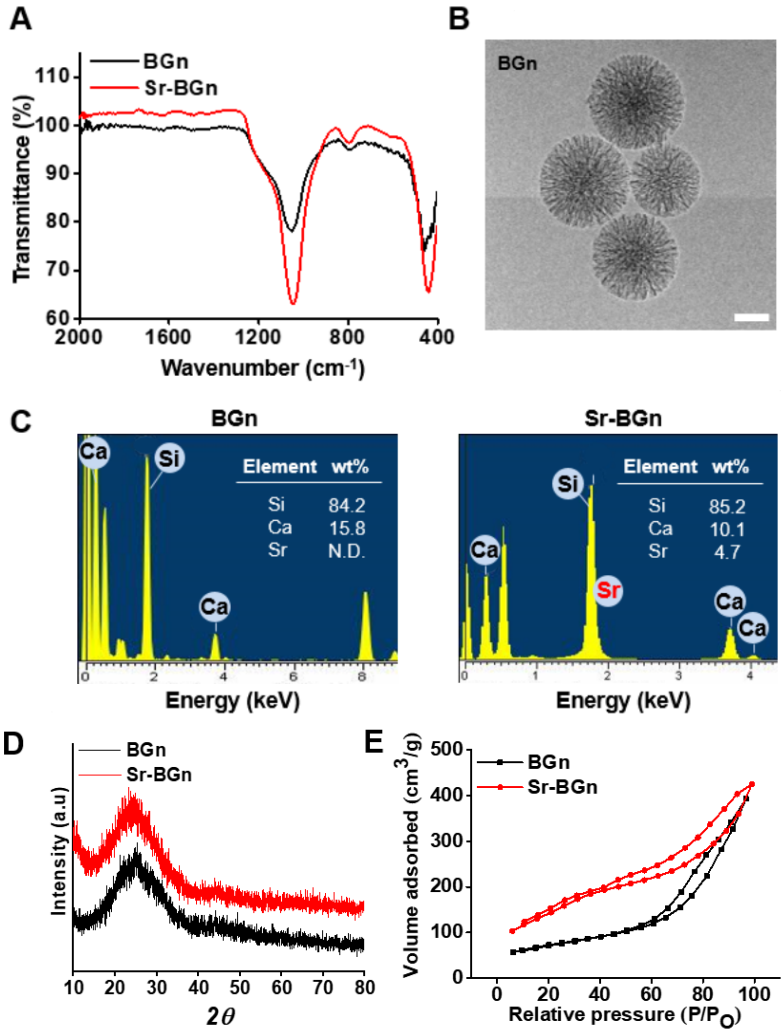

F

	BGn	Sr-BGn
Surface area (m^2/g)	620.9	693.0
Ave. pore size (nm)	6.72	6.64
Total pore volume (cm^3/g)	0.56	0.61
ξ-potential (mV)	-10.1±0.3	-15.6±3.4

Figure S1. Characteristics of nanoglasses (BGn and Sr-BGn). (A) FT-IR spectra, (B) TEM image of BGn (scale bar = 100 nm), (C) EDS spectra, (D) XRD patterns. XRD patterns indicate the amorphous phase of nanoglass samples, (E) BET nitrogen adsorption/desorption curves, (F) summary of properties including surface area, average pore size, total pore volume and zeta-potential.

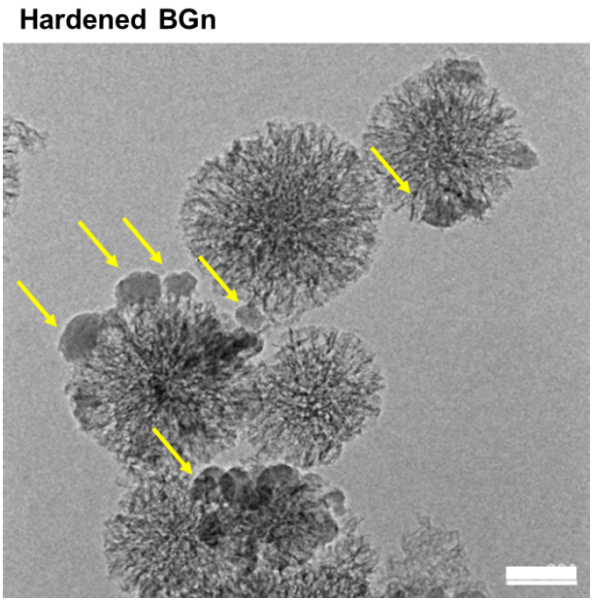

Figure S2. TEM image of BGn during setting reaction (scale bar = 100 nm). Arrows indicate nano-precipitates formed on the surface of the nanoparticles.

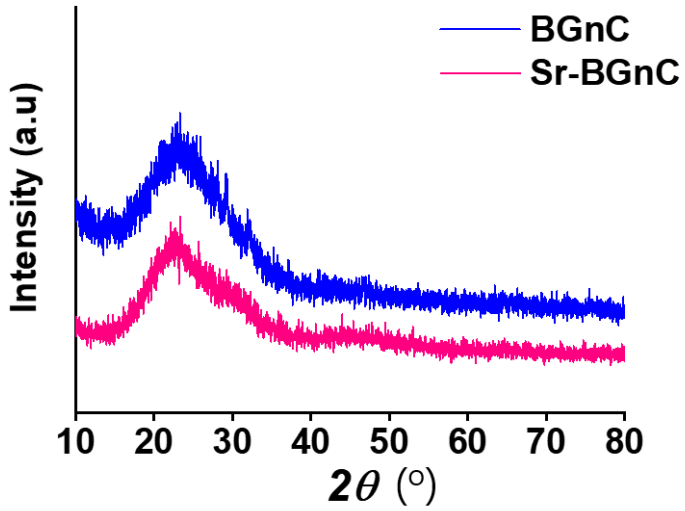

Figure S3. XRD patterns of the nanocements after cementation.

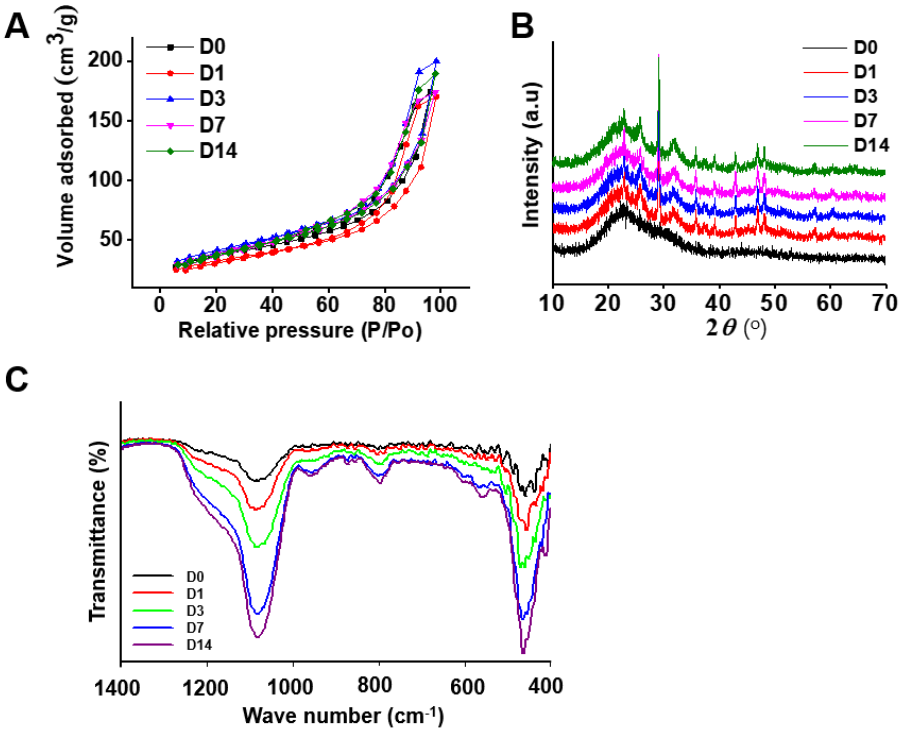

Figure S4. Analyses of Sr-BGnC after mineralization in SBF for different periods: (A) BET, (B) XRD, and (C) FT-IR.

Table S1. Ionic extracts from the nanocement samples used for cell cultures.

ppm	Sr^{2+}	Ca^{2+}	Silicate
BGnC	-	86.24 (±2.83)	21.50 (±8.59)
Sr-BGnC	12.18 (±0.73)	74.66 (±0.93)	22.73 (±7.62)

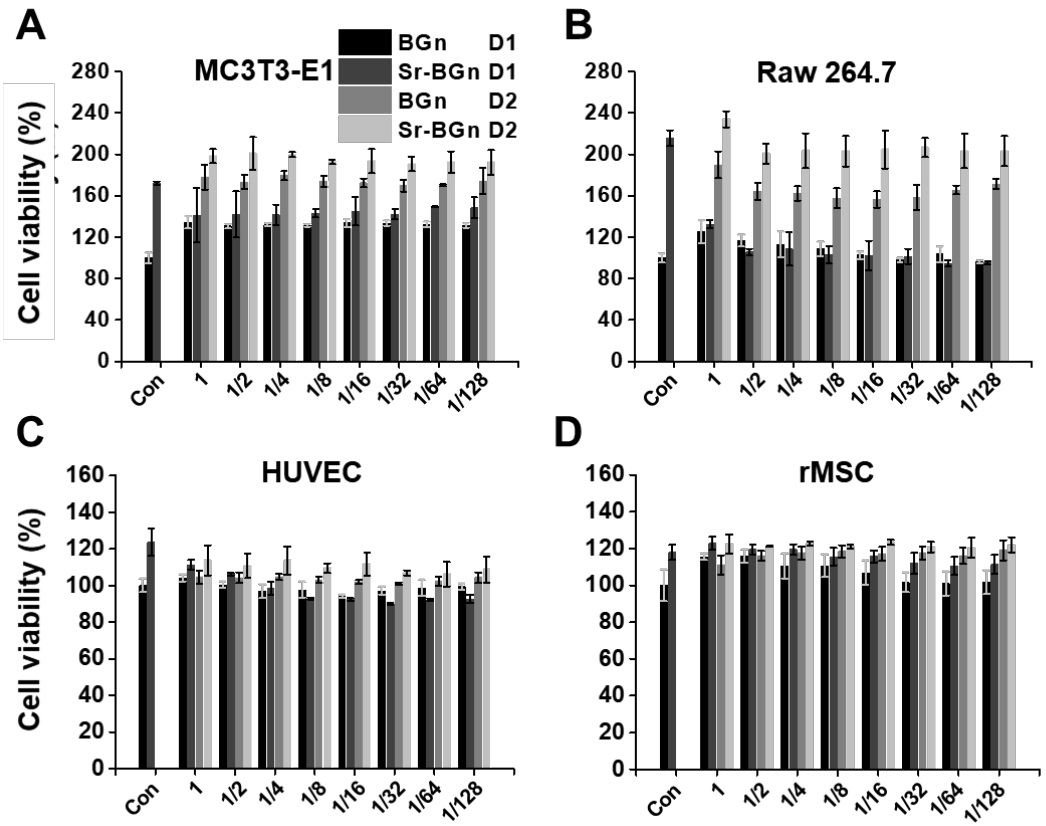

Figure S5. In vitro cell viability on the nanocements prepared at various extract dilutions. Cell viability tested with MC3T3-E1 (A), RAW264.7 (B), HUVEC (C) and rat MSC (D) treated with the nanocement extracts for 1 day or 2 days. Serial dilutes (from 1/2 to 1/128) were treated to cells.

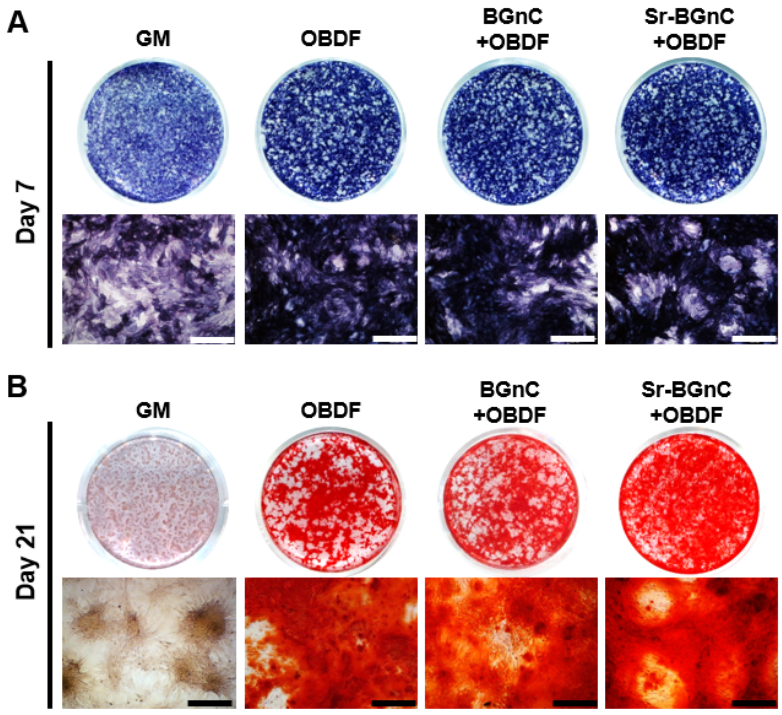

Figure S6. Effects of nanocements on osteogenic differentiation of rat MSCs: (A) ALP at day 7, and (B) ARS at day 21.

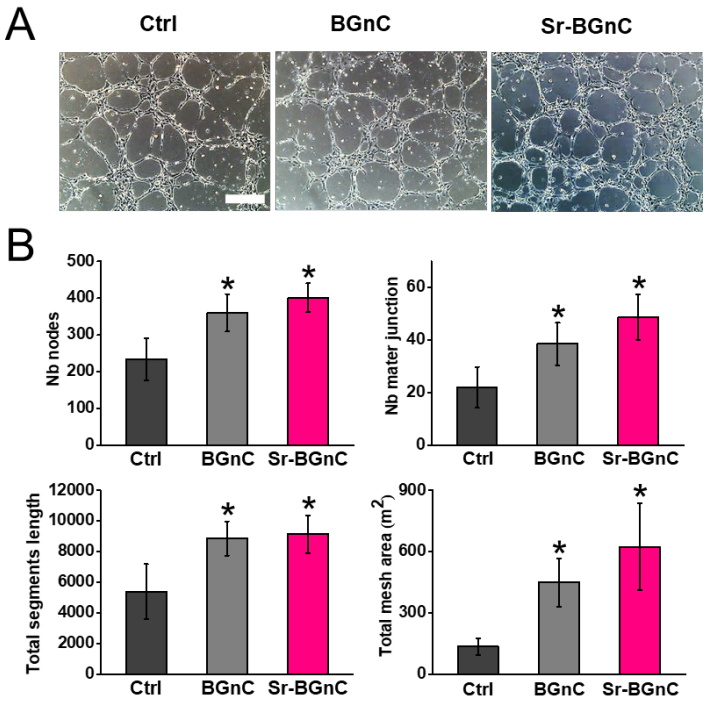

Figure S7. In vitro pro-angiogenic capacity of Sr-BGnC. The nanocement extracts were treated to HUVECs seeded on a Matrigel-coated plate for 3 h. (A) Optical images of the tubule formation. (B) Image analysis results of the number of node and node master junction, total segments length and total mesh area. *$p<0.05$ *versus* control (Ctrl).

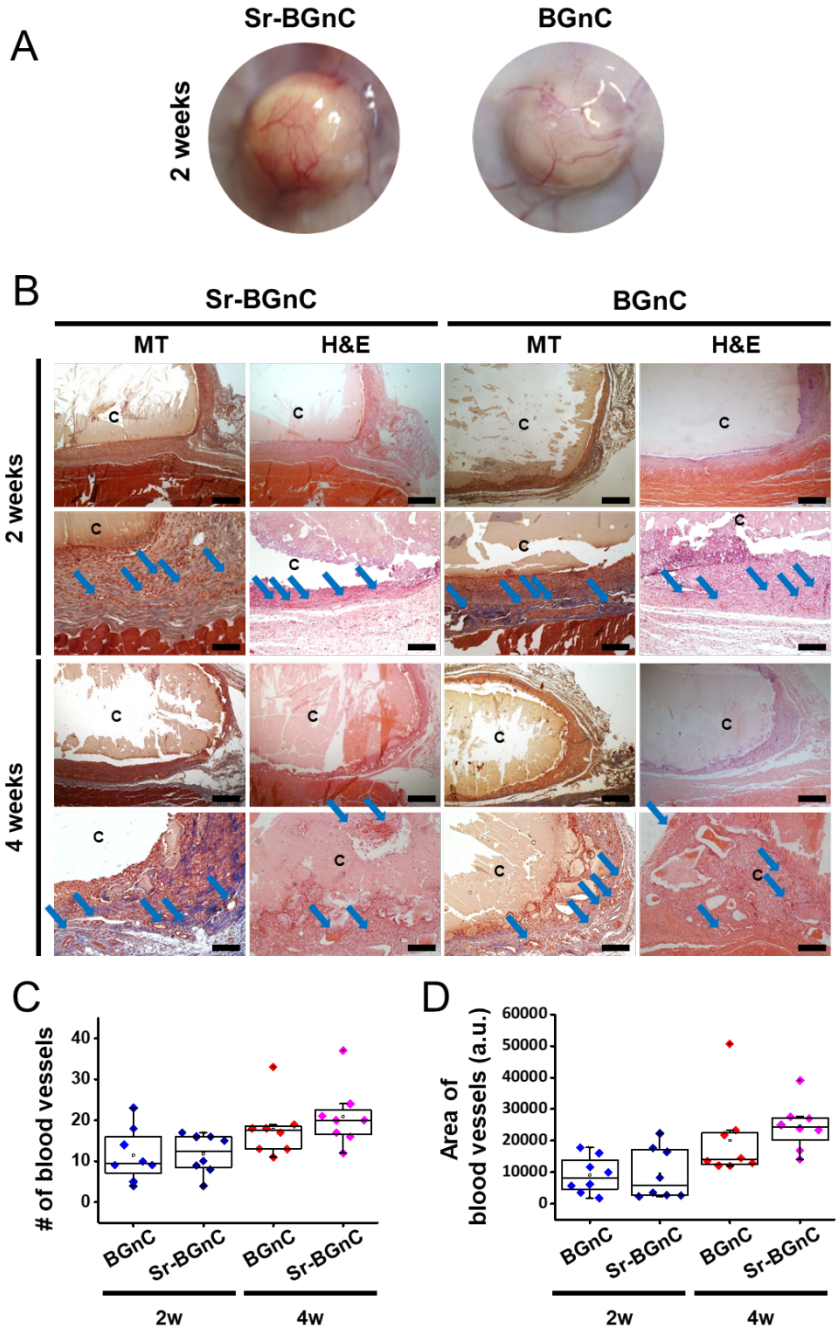

Figure S8. *In vivo* tissue compatibility and pro-angiogenic capacity of Sr-BGnC assessed in rat subcutaneous tissue. The implanted nanocements were harvested at 2- and 4-week post-implantation; (A) Gross images at 2 weeks, and (B) histological analyses by Masson's trichrome (MT) and H&E staining (scale bar = 500 μm and 200 μm in low and high magnification images, respectively). 'c' is implanted area, and blue arrows indicate neo-blood vessels. The number (C) and area (D) of blood vessels were analyzed by Image J.

Table S2. Summary of experimental details of the in vitro cell studies.

Target	Figure	Cell type	Culture media	Experiment details
Osteogenesis	Fig.2	MC3T3-E1	Nanocement extracts + OBDF	Osteogenic differentiation capacity of nanocement extracts (gene expression, ALP & ARS staining, Luciferase assay)
Inhibition of osteoclastogenesis	Fig.3	RAW 264.7	Nanocement extracts + OCDF	Inhibitory effects of nanocement extracts on osteoclast differentiation (gene expression, Actin ring formation, TRAP staining, Pit assay)
Inhibition of osteoclastogenesis	Fig.4	RAW 264.7	Osteoblasts conditioned media + OCDF	Inhibitory effects of conditioned medium extracts on osteoclast differentiation (Luciferase assay, gene expression, TRAP staining, Pit assay)
Mechanism	Fig.5	RAW 264.7	Osteoblasts conditioned media + OCDF	Mechanism study of Inhibitory effects of conditioned medium extracts on osteoclast differentiation (ELISA, Western blot)

Abbreviations: OBDF; osteoblast differentiation factors, OCDF; osteoclast differentiation factors, ALP; alkaline phosphatase, ARS; alizarin red S, TRAP; Tartrate-resistant acid phosphatase, ELISA; enzyme-linked immunosorbent assay.